

CHAPTER 7

Applications of Electron Microscopy in Heterogeneous Catalysis

Yuyuan Lin*, James A. McCarthy, Kenneth R. Poeppelmeier, Laurence D. Marks

Northwestern University, Evanston, IL, USA

*Corresponding author: E-mail: linyuyuan630@gmail.com

LIST OF ABBREVIATIONS

| | |
|--------------|--|
| ABF | Annular bright field |
| ADF | Annular dark field |
| AFM | Atomic force microscopy |
| BF | Bright field |
| CCD | Charge coupled device |
| DF | Dark field |
| DFT | Density functional theory |
| EELS | Electron energy loss spectroscopy |
| EDS | Energy-dispersive X-ray spectroscopy |
| ETEM | Environmental transmission electron microscopy |
| FT-IR | Fourier transform infrared |
| GNP | Gold nanoparticle |
| HAADF | High angle annular dark field |
| HOR | Hydrogen oxidation reaction |
| HREM | High-resolution electron microscopy |
| IR | Infrared |
| LB | Langmuir–Boldgett |
| NPG | Nanoporous gold |
| ORR | Oxygen reduction reaction |
| PEEM | Photoelectron electron microscopy |
| PEM | Proton exchange membrane |
| PROX | Preferential CO oxidation in excess hydrogen |
| REM | Reflection electron microscopy |
| SACs | Single atom catalysts |
| SEM | Scanning electron microscopy |
| SOFC | Solid oxide fuel cell |
| STEM | Scanning transmission electron microscopy |
| STM | Scanning tunneling microscopy |
| TEM | Transmission electron microscopy |
| UHV | Ultra-high vacuum |
| WGS | Water gas shift |
| XRD | X-ray diffraction |

1. INTRODUCTION

A good catalyst should have high activity, selectivity, and stability as well as low economic and environmental costs. Owing to the development of controlled synthetic methods, catalysts with novel chemical and morphological designs have been found to enhance catalytic properties. For example, catalytic systems with well-defined shapes, bimetallic catalysts, core-shell nanoparticles, and single atom catalysts have been obtained by a variety of chemical and physical preparation methods. Those systems offer unique advantages for optimizing catalytic performance. On the other hand, direct characterization of the catalysts at the nanoscale or atomic scale can help to verify the rational design and provide a mechanistic understanding. A clear mechanism in turn can aid in the development of future catalysts.

Transmission electron microscopy (TEM) is one of the most often used techniques for characterization of catalysts, and can provide rich information about the morphology, structure, and chemical composition. TEM has undergone great improvements in resolution and functionality since the first one was built by Max Knoll and Ernst Ruska in 1931. Figure 1 shows the historical improvement of the best point-to-point resolution in TEM. The development of the TEM design, electron gun, vacuum, aberration correctors, and other components has led to some microscopes with sub-Å resolution.

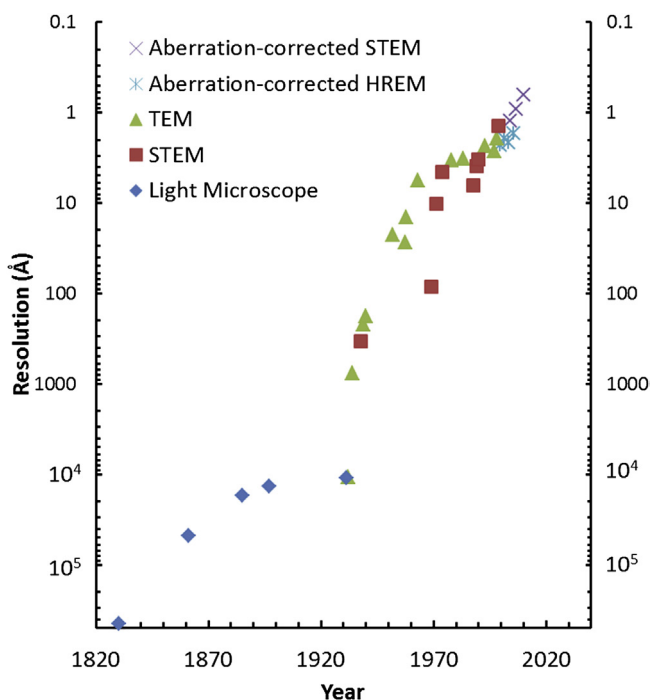


Figure 1 Chronological advancement of microscope resolution. *Reproduced from S.J. Pennycook et al. in: A.V. Narlikar, Y.Y. Fu, (Eds.), The Oxford Handbook of Nanoscience and Nanotechnology, Oxford University Press, Oxford, United Kingdom (2010) p. 205.*

Understanding catalysts at the atomic level is no longer limited to the model extended surfaces on single crystals using conventional surface-sensitive techniques. Imaging the active surface sites of real catalytic nanoparticles can now be achieved by operating TEM in high resolution electron microscopy (HREM) and scanning transmission electron microscopy (STEM) modes. Hence the materials gap in the characterization of catalysts can be bridged by performing TEM characterization. Recently it has been reported that the secondary electrons signals generated by the STEM electron probe can achieve atomic resolution [1]. This is essentially the same as performing scanning electron microscopy (SEM) in a TEM, and it has a promising future for studying the surfaces of materials. In addition to advanced imaging techniques, modern TEMs are often equipped with energy dispersive X-ray spectroscopy (EDS) and/or electron energy loss spectroscopy (EELS), which can help to analyze the local chemical composition of materials. Advances in TEM have also increased the spatial resolution and energy resolution of EDS and EELS. The combination of imaging and spectroscopic studies often results in a more conclusive interpretation. Furthermore, a functional TEM holder or an environmental TEM (ETEM) enables the in situ characterization of materials under different gaseous environments and/or at elevated temperatures. The pressure in a typical TEM column is $\sim 10^{-7}$ Torr while ETEM can be operated under a pressure of up to ~ 20 Torr [2]. Therefore, performing direct TEM studies can bridge the pressure gap between ultra-high vacuum (UHV) surface science and realistic gaseous conditions.

Rather than a comprehensive introduction to TEM, the purpose of the TEM part of this chapter is to provide an understanding of image contrast in HREM and STEM. Furthermore, an additional aim of this part is to illustrate how to correctly interpret atomic resolution TEM images. Several recent applications of TEM in studies of heterogeneous catalysis are discussed in the case study section. In addition to illustrating the structural and chemical information included in the images, topics including oxide surface stabilization mechanisms, catalytic reaction mechanisms, nanostructure syntheses, and equilibrium metal shapes will be briefly discussed in the case studies. For the readers who are interested in a more detailed knowledge of TEM, there are several excellent textbooks available [3–5]. As stressed by many researchers within the field, a better understating of catalysis should always combine the results of different characterization methods. Other techniques including Fourier transform infrared spectroscopy (FT-IR), Raman spectroscopy, extended X-ray absorption fine structure (EXAFS), and density functional theory (DFT) should often be used to confirm the structural or chemical information provided by TEM images.

2. BASICS OF TEM

The wealth of information TEM can provide is due to the different electron-specimen interactions and versatility of TEM operation methods. Figure 2(A) shows a cross-sectional view of a simplified TEM model. Changing the convergence of the illuminating beam

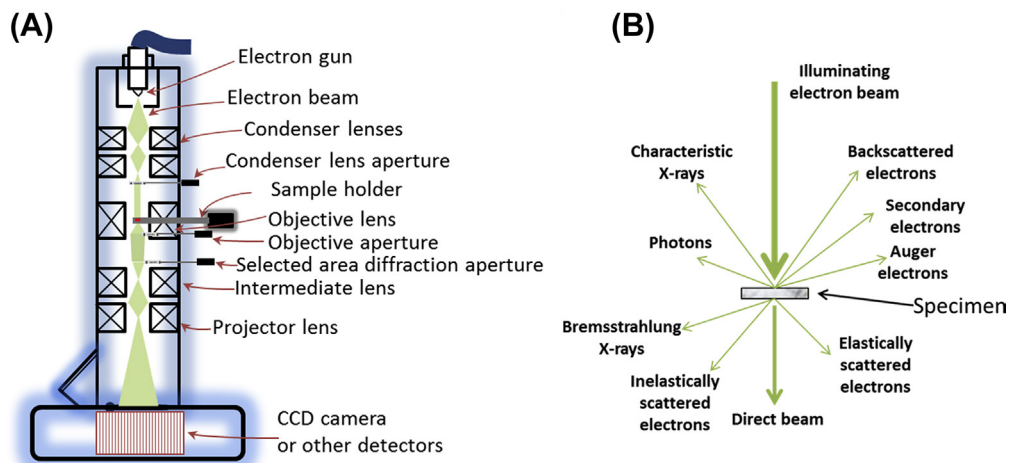


Figure 2 Basics of transmission electron microscopy (TEM): (A) Schematic setup of TEM, and (B) signals generated when high-energy electrons interact with a specimen.

and using different apertures or detectors can lead to different operating modes for specific applications. Figure 2(B) shows different types of signals generated by a high energy electron beam (usually 80–300 KeV) passing through a thin specimen. Images are formed by the detection of transmitted beams. The objective lens aperture can be used to selectively choose the direct beam to form images, which are known as bright field (BF) images. If the scattered electrons are chosen, the corresponding images are dark field (DF) images. The BF and DF images sometimes are very useful to deliberately enhance or suppress signals of a particular material, crystal plane, or defects. Analyzing the energy loss of the inelastically scattered beam can help to determine the elemental composition and bonding configurations of materials, which is the principle of EELS. Above the specimen, the characteristic X-ray signals can be utilized for EDS analysis. Collecting the signals of the secondary electrons and backscattered electrons can form surface-sensitive SEM-like images.

In imaging techniques, an important issue is the image contrast. The contrast can be understood as the differentiation of the object of interest from the background due to differences in intensity (brightness or darkness). Whether the object is brighter or darker than the background depends on the TEM operation and the materials themselves. A common feature of BF images is that the vacuum is whiter than the specimen. In contrast, the vacuum is black in DF images as the direct beam is blocked by the apertures.

The two most often used operation modes for atomic resolution imaging are HREM and STEM. Figure 3 shows a comparison between STEM mode and HREM mode. In STEM mode, the electron beam converges to a probe (typically close to 1 Å to obtain atomic resolution) which scans across the sample, while HREM makes use of static

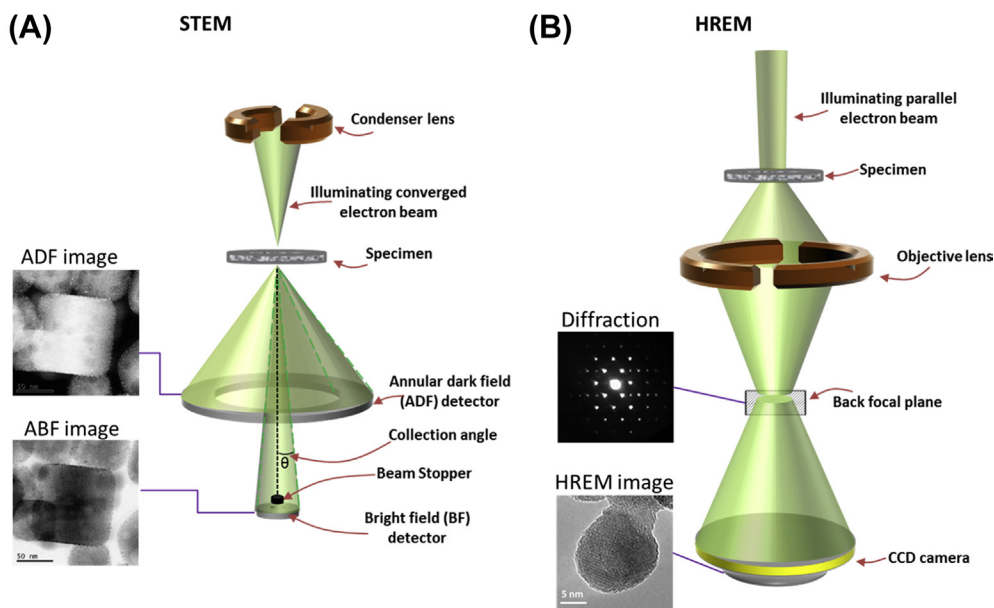


Figure 3 Comparison of image formation in scanning transmission electron microscopy (STEM) and high resolution electron microscopy (HREM). (A) Schematic view of image formation in STEM mode. (B) Schematic showing image formation in HREM mode.

parallel beam imaging. In STEM mode, after the electrons exit the sample, the scattered beams and direct beam can be collected in the diffraction plane by annular detectors. The analog signal on each detector is digitalized and displayed on the computer screen. The electrons collected by the annular dark field detectors (ADF) can form images in which the contrast is related to the atomic number of the materials. Usually the larger Z is, the brighter the material appears in the Z -contrast ADF images while the vacuum is displayed as a black background. The Z -dependency can be tuned by the collection angle of annular detectors. For example, increasing the collection angle (θ) of ADF detectors increases the Z -dependency of the image contrast. The detector with collection angle larger than 50 mrad is considered to be a high angle ADF (HAADF) detector. For HAADF images, the contrast is proportional to Z^n (n can be ~ 1.7), and thus the HAADF images are often called Z -contrast images. The direct beam and scattered beams within a very small angle can be collected by the bright field (BF) detector. Usually the collection angle for BF detector is less than 10 mrad. If a beam stop is used with the BF detector to block the direct electrons, the resulting images are called annular bright field (ABF) images. Typically in HREM mode, all of the signals in the diffraction plane pass through additional TEM lenses and form an HREM image on a CCD camera. Selectively allowing the direct or diffracted spots in the diffraction plane to pass through the remaining lens optics can form BF or DF images, respectively. The lattice

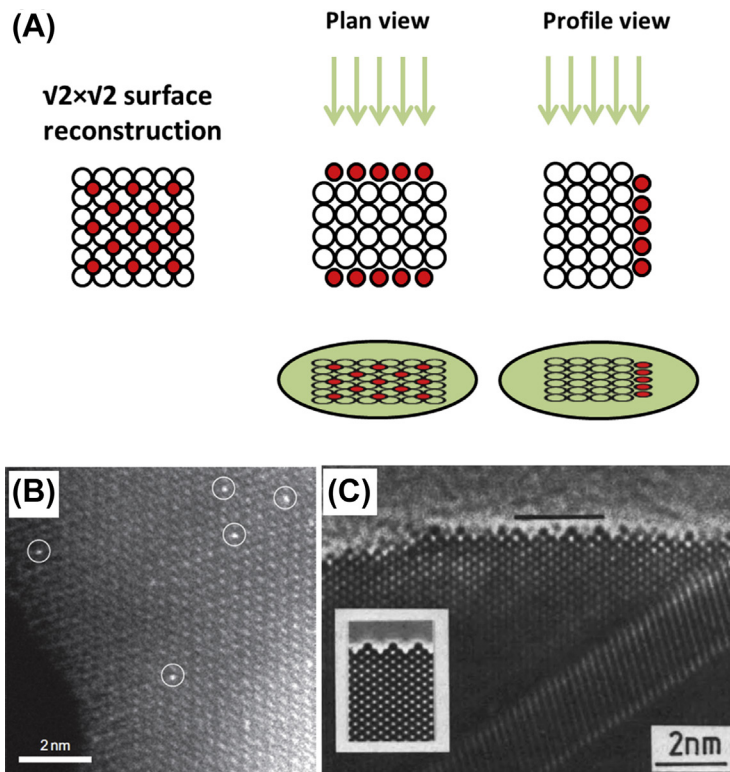


Figure 4 Illustration of plan-view and profile-view surface imaging modes in transmission electron microscopy. (A) Schematic view of the plan-view and profile-view imaging. (B) A high angle annular dark field image in plan-view mode showing single Pt atoms dispersed on a FeO_x support. (C) A profile-view high resolution electron microscopy image showing a (2 × 1) surface reconstruction on an Au (110) surface. The simulated image is shown in the inset. Panel (B) was reprinted by permission from Macmillan Publishers Ltd: Qiao et al. *Nat. Chem.* 3 (2011) 634–641, copyright 2011.

fringes in HREM images are a result of the interference between the direct and diffracted spots. In STEM, as the collection angle of the BF detector is small enough so that the beam can be considered a parallel beam, BF-STEM and HREM are related by reciprocity and thus the mechanisms of image contrast are identical if inelastic scattering is minimal [6].

Most TEM images can be considered as projections of a 3D object. Thus TEM images contain both bulk and surface information about materials. In heterogeneous catalysis, the surface structures of catalysts and supports are of particular interest. By tilting the specimen to a direction (plane normal) parallel or perpendicular to the beam direction, the surface information can be visualized in plan view and profile view, as shown in Figure 4(A). The plan-view images in TEM of 3D materials have signal overlap between the bulk and surface. Plan-view imaging is useful when the surface has a different

structure/material from the bulk structures. For example, a supported single atom catalyst site can be readily distinguished from the support, as shown in Figure 4(B) [7]. If a surface reconstruction is present, the reconstructed surface structure can be abstracted by filtering out the bulk information using imaging processing [8,9]. In the case when the supported metal particles and supports are crystalline, the metal-support interface structure can be analyzed by the Moiré patterns [10]. A Moiré pattern is generated when two periodic patterns overlap.

In profile-view mode, the surface and bulk are separated. Sometimes the surface structures as well as the registry to the bulk can be conveniently imaged. The first profile imaging was reported by Marks and Smith in 1983 using conventional HREM [11] (Figure 4(C)), and they found a (2×1) reconstructed (110) surface of Au nanoparticles. Particularly after the implementation of aberration correctors for HREM images, light elements such as O atoms were able to be imaged clearly. The atomic surface structures of Co_3O_4 [12], CeO_2 [13], SrTiO_3 [14] nanoparticles as well as other materials [15–18] have been solved using profile-view mode in the past few years. A drawback is that the 2D surface structure is displayed as a 1D edge-on contrast, as shown in Figure 4(A). It is very difficult to image the 2D surface defect structures as conventional scanning tunneling microscopy (STM) or atomic force microscopy (AFM) does. The reduction of dimensionality can also result in misinterpretations. For example, a reconstructed $(\sqrt{2} \times \sqrt{2})$ surface structure can show up as a (1×1) surface. Therefore, image simulation as well as imaging in a different crystal zone axis can often differentiate the correct surface structures from the other possible ones.

3. ATOMIC RESOLUTION CHARACTERIZATION USING TEM

3.1 Aberration Correction

Similar to optical lenses, the magnetic lens in TEM is not perfect. Lens artifacts such as astigmatisms, coma, spherical aberration (Cs), and chromatic aberration which exist in glass lenses also exist in the electromagnetic lens of a TEM. For STEM mode, the aberrations in the condenser lens are the most important, while in HREM mode, the aberrations of the objective lens are the most important. The aberrations can reduce the image resolution and increase the difficulty of interpreting image contrast. A significant obstacle that limits the resolution of TEM images is Cs. Cs can be understood as the edge of a converging lens always bending the transmitting beam too much such that the beam cannot be brought to a focal spot, as shown in Figure 5. The nonuniform focal plane causes blurriness and increases the complexity. The concept Cs correction was first suggested by Scherzer [19] and further developed Crewe, Rose, Haider, Krivanek, et al. [20,21]. For a glass lens, the Cs can be corrected by using a diverging lens. An “effective” diverging lens can be created in TEM by using non-cylindrical lenses such as octapoles, which are used for Cs correction.

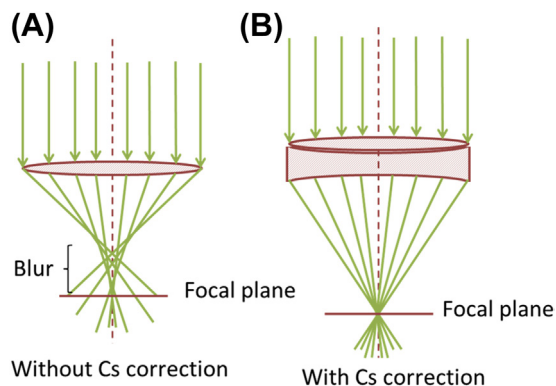


Figure 5 Schematic illustration of Cs and Cs correction. (A) A lens with Cs. (B) A lens with Cs corrected by a diverging lens.

Correction of chromatic aberration (Cc) can further increase the resolution and interpretability of TEM images. The unstable electron gun source can generate electrons with different energies, as can instabilities in the high voltage source and inelastic scattering in the sample. The lens in TEM bends the electrons differently due to the different energies. The resulting nonuniform focal plane for the electrons is what limits the resolution. The principle of Cc correction is similar to Cs correction. An “effective” diverging lens can be used to bend the electron beams to the same focal plane. With both Cc and Cs correction, the best point-to-point resolution that has been achieved is close to 0.5 \AA [22].

3.2 Resolution and Precision

The point-to-point resolution (ρ) in TEM can be defined as the smallest observable distance between two objects. Modern advances in TEM design have improved the point-to-point resolution to 0.5 \AA . For simplicity, consider the objects as Gaussian functions as shown in Figure 6. If the two Gaussian functions start to overlap, the resolution of the functions worsens. At the point when the total intensity of the two overlapping functions is $\sim 25\%$ less than the peak intensity of the individual functions, the distance between the two peaks meets the Rayleigh criterion for resolution (best point-to-point resolution). We can see that resolution has a subjective definition. There is no strict requirement for the intensity of the overlapping area. For aberration-corrected microscopes the resolution can be below 1 \AA , which allows for visualization of separated atom columns of most crystals in low index zone axes.

Precision (σ) is related to resolution by $\sigma = \frac{\rho}{\sqrt{N}}$, where N is the total electron dose for the object. For a typical HREM image taken with a modern aberration-corrected electron microscope, the electron dose is $500\text{--}40,000 \text{ e}/\text{\AA}^2\text{s}$. Assuming a resolution of 0.8 \AA and a Gaussian function width of 1 \AA , the precision can be $0.036\text{--}0.004 \text{ \AA}$. That is

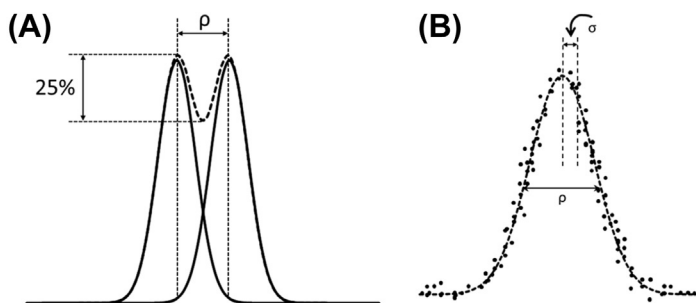


Figure 6 Comparison of resolution and precision. (A) The point-to-point resolution defined as the Rayleigh criterion. (B) Illustration of the definition of precision. The precision of peak position (σ) is related to both resolution and signal-to-noise ratio.

why some HREM images can predict atomic locations at the picometer scale, which is very useful for measuring lattice relaxations. For example, Yu et al. showed that the surface plane of Co_3O_4 (111) has an inward contraction of 20 pm [12]. When comparing two images, it is possible that one has a worse resolution but a better precision if it has a high signal-to-noise ratio. Hence resolution is not the only concern in microscopic studies.

3.3 Atom Locations STEM and HREM Images

In both STEM and HREM images, the contrast is a combined result of the intrinsic electron-specimen interaction and the electron-lens interaction. We can “see” atoms in “good” HREM or STEM images because the electron-specimen interaction is localized around the atoms, that is, good localization. In a crystalline specimen, the electron signals are mostly confined around the atom columns instead of undergoing diffuse scattering. The well-defined atom columns can be observed by tilting the crystalline specimen to a low index zone axis. We generally want the TEM lens to magnify the images and enhance the contrast, but to not influence the relative localization of the projected atom positions. The following content intuitively illustrates the atom locations in HREM and STEM images.

3.3.1 High Resolution Electron Microscopy

As long as TEM has a coherent illuminating electron source, obtaining an HREM image with lattice fringes is not difficult. The spacing of the lattice fringes indicates the distance between crystallographic lattice planes (d -spacing), which is very useful for characterizing the structure of a specimen. However, interpretation of HREM contrast beyond d -spacing is not trivial. The spots (either bright or dark spots) can represent real atoms or may just be artifacts. In HREM, both the intrinsic electron-specimen interaction and the electron-lens interaction can cause the atoms to appear as white or black spots in the images. The electron-specimen interaction and electron-lens interaction can be

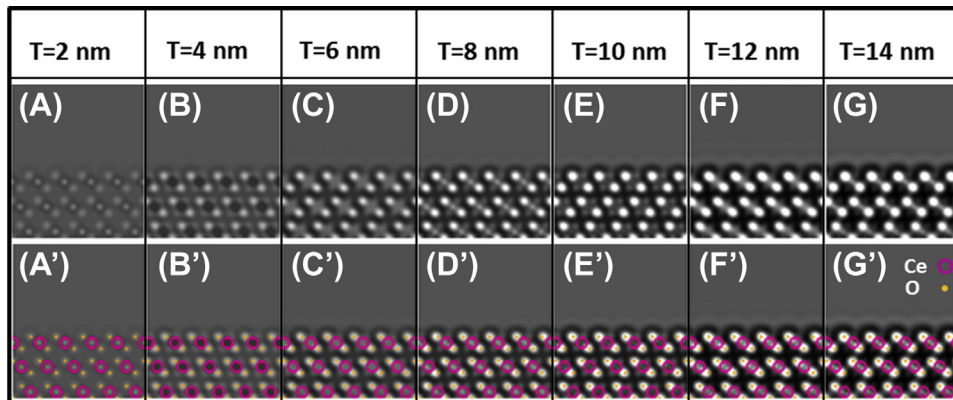


Figure 7 (A)–(G) Simulated high resolution electron microscopy images of the CeO_2 (111) surface with varying thicknesses at a fixed defocus (2 nm). The atom locations of each image are shown in (A')–(G'), respectively.

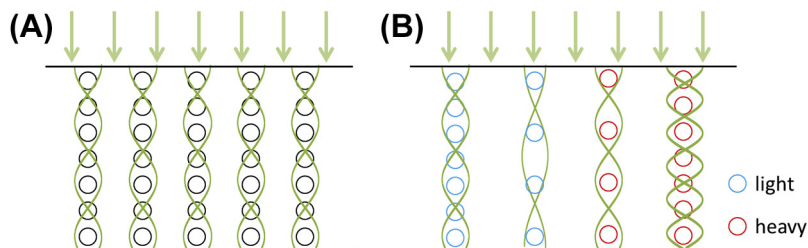


Figure 8 Schematic illustration of electron channeling theory in high resolution electron microscopy. (A) Channeling in a crystal. (B) Channeling along different atom columns. *Reproduced from D. Van Dyck, M. Op de Beeck, Ultramicroscopy 64 (1996) 99–107.*

simplified to the thickness effect and lens defocus effect, respectively. [Figure 7](#) shows simulated HREM images for CeO_2 (111) surfaces with varying thicknesses and a fixed defocus. When the specimen thickness is 2 nm ($T = 2$ nm), both Ce and O atoms appear as white spots (see [Figure 7\(A\)](#) and (A')). As the thickness increases, the intensity of Ce positions oscillates from white to black. The intensity of the O positions increases but the contrast is maintained as white spots.

The thickness dependence of HREM contrast arises from the complex interaction between the direct transmitting beam and diffracted beam in the specimen, which can be intuitively understood by the s -state electron channeling model [23]. When a crystal is tilted to a zone axis, the atoms are aligned into columns along the electron beams, as shown in [Figure 8\(A\)](#). After the electrons reach the sample, the dominant electron scattering is confined to the channels provided by the atoms in the material owing to the electron-atom interactions. The intensity of the electron wave along each atom column oscillates with a certain periodicity. Thus the intensity of the wave as it exits the material is dependent on the material thickness. Furthermore, the intensity of the exit wave is

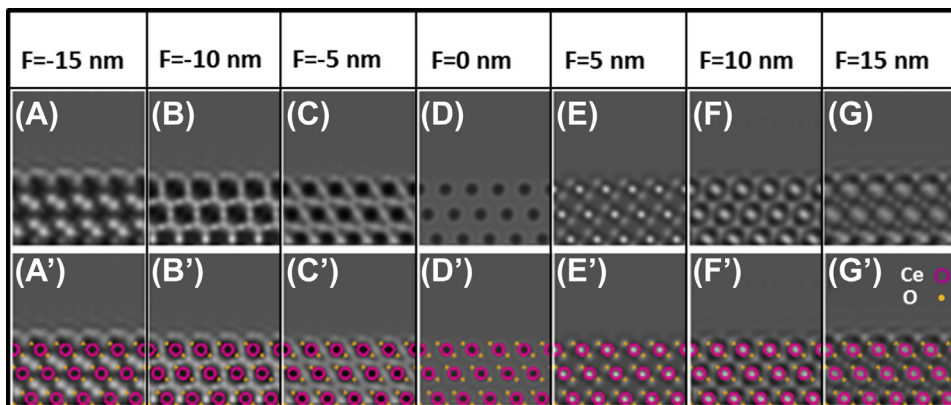


Figure 9 Simulated high resolution electron microscopy images of the CeO_2 (111) surface with varying degrees of defocus at a fixed thickness (2 nm). The atom locations for each image are shown in (A')–(G'), respectively.

zone-axis dependent and element dependent, as shown in [Figure 8\(B\)](#). For a zone axis along which the atoms are packed sparsely, the oscillation is slower than in the columns where atoms are packed closely. With the same thickness and same atom density within atom columns, an electron wave traveling along a “heavy” element column will oscillate faster than one traveling along a column containing lighter elements. Therefore, a significant advantage of HREM is that even in the presence of heavy elements, light elements can still be visualized for a specimen with a certain thickness.

To understand the defocus effect on HREM images, we can again use the CeO_2 (111) surface as an example. [Figure 9](#) shows a 2 nm thick CeO_2 sample with varying defocus values ranging from -15 to 15 nm. Several impacts of defocus on the images can be summarized based on [Figure 9](#). (1) Small defocus results in good image localization. At small defocus such as $F = 5$ nm, the spots in the images directly correspond to atom locations. At a defocus of 15 nm, it is hard to relate the image contrast to atom positions. Particularly for the surface, additional fringes (Fresnel fringes) other than those representing real atom contrast (visible at the surface areas of [Figure 9\(A\)](#) and [\(G\)](#)) can make the interpretation of surface contrast very difficult. (2) Positive defocus and negative defocus can reverse the image contrast. For $F = -5$ nm, the black spots are atoms. However, at $F = 5$ nm, the O and Ce atoms appear as white spots. (3) Zero defocus is not necessarily the best imaging condition. The image with $F = 5$ nm has a better contrast than the image with $F = 0$ nm. According to HREM theory, zero aberration results in an image with minimal contrast for a thin specimen although the image localization is optimized. The “best” image is a balance between localization and image contrast. Sometimes a small defocus or Cs is intentionally applied to obtain images with good contrast [24]. Nevertheless, a minimal contrast image is very useful in practice, as it is a way to identify the zero defocus condition. The absolute values of defocus can then be approximately determined based on the zero defocus reference.

Defocus is not the only aberration. There are other aberrations such as astigmatisms, coma, and Cs, all of which can induce delocalization and render the HREM images difficult to interpret. Fortunately, for HREM imaging there are many simulation programs [25–30] which work quite well, and the computational time for each simulation is very fast (several seconds). In a typical simulation program, besides the sample structure, imaging parameter inputs such as the defocus, Cs, sample thickness, astigmatism, and sample tilt are all required as input parameters to generate simulated HREM images. Better control of imaging parameters in an HREM experiment facilitates the simulation processes, although sometimes it is hard to know the correct values to use.

3.3.2 Scanning Transmission Electron Microscopy

When the electron beam converges to a probe with a size on the atomic scale, atomic resolution imaging is possible. However, the contrast differs considerably between BF, ABF, ADF, and HAADF images in STEM. A BF-STEM image should be understood (by reciprocity) as an HREM image. The changing of specimen thickness and defocus can cause contrast reversal in the atom positions. In ADF images, good image localization at atom positions is also due to s-state channeling although changes in orientation (strain) can also lead to significant contrast. In general it is better to use larger collection angles, that is, HAADF, in order to minimize this, although it can never be completely eliminated. However, the behavior of the electron channeling differs between ADF and particularly HAADF and HREM. In HAADF, the intensity of the spots only slightly changes with the specimen thickness. There is no contrast reversal with respect to the thickness change provided the thickness is not too large. The atoms in HAADF images appear as white spots in most cases. The aberrations such as defocus can also induce significant delocalization in HAADF images. However, the contrast will not reverse as in HREM. The atoms remain white as the defocus changes in HAADF images.

The significant difference between ADF/HAADF and BF images arises from the direct beam which is collected by the BF detector. In principle, if the direct beam is blocked, the interference between the direct and diffracted beams in the specimen can be neglected. In practice, a beam stopper can be put on top of the BF detector to block the direct beam. The resulting images collected by the BF detector are ABF images. The ABF technique has the same advantage as HAADF in that it has relatively low sensitivity to specimen thickness and defocus compared to HREM. In addition, it has good sensitivity to both heavy and light elements, similar to BF imaging. Intuitively, as the large angle scattered beam (the electrons collected by HAADF) is not collected, the atoms appear black in ABF. Experimental and simulated ABF images on several materials all demonstrated that the ABF technique is less sensitive to thickness and defocus [31,32]. Examples of HAADF and ABF images of four different materials [31] are shown in [Figure 10](#).

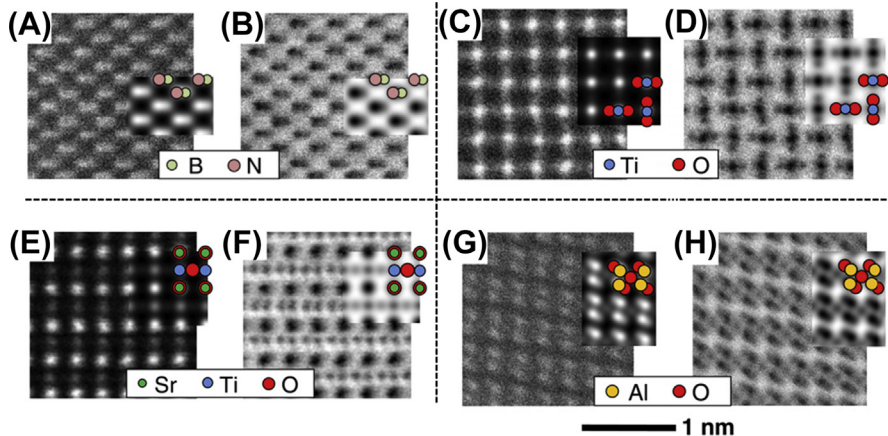


Figure 10 Comparison of high angle annular dark field and annular bright field images of (A), (B) cubic BN [110], (C), (D) TiO_2 [001], (E), (F) SrTiO_3 [011], and (G), (H) Al_2O_3 [$\bar{1}210$]. The simulated images are shown in the insets with the structural models overlaid. Reprinted from Findlay et al. *Dynamics of annular bright field imaging in scanning transmission electron microscopy*, *Ultramicroscopy* 110 903–923, Copyright (2010), with permission from Elsevier.

Although the interpretation of HAADF and ABF images is relatively easy, sometimes image simulations are necessary, particularly for two materials with different thickness. In HAADF images, the “Z-contrast” is only for specimen with same imaging condition (such as thickness and defocus). For two species in a specimen with different thicknesses, the intensity is not necessarily directly related to Z. The popular HREM simulation programs usually contain a package for STEM simulation. The simulation of STEM images usually requires more computational time than HREM simulation.

3.3.3 HREM versus STEM

HREM, ADF-, ABF-, and BF-STEM techniques are all capable of imaging atoms. Operation in STEM mode allows users to obtain images with a desired contrast. Most often the HAADF-STEM images are Z-contrast images, which can significantly facilitate image interpretation. However, HAADF-STEM has relatively low sensitivity to light elements when heavy elements are present. ABF- and BF-STEM can image the light and heavy atoms simultaneously. The contrast in BF-STEM and HREM images can reverse with respect to thickness and defocus. Performing image simulation is very important to correctly interpret the images.

In practice, the HAADF and BF signals can often be obtained simultaneously. Or for a microscope equipped with EDS or EELS, operating in STEM mode significantly enhances the spatial resolution of elemental analysis. This is very helpful for visualizing some systems such as bimetallic catalysts in which each element cannot be identified easily using imaging techniques. In some other aspects HREM has advantages over

HAADF. Usually HREM utilizes all the electrons passing through the specimen, so the signal-to-noise ratio is higher than in HAADF. The high signal-to-noise ratio in some cases is very important for imaging the surface structures. Specimen drift should also be considered in order to choose the right imaging mode. For example, specimen drift during the scanning of the electron probe results in distorted atom column positions in an STEM image for both BF and HAADF. Hence the measurement of surface relaxation typically involves more noise or errors in STEM than in HREM.

4. CASE STUDIES

4.1 Atomic Surface Structures of Well-Defined Oxide Supports

4.1.1 CeO_2 Nanocubes

Owing to its remarkable redox ability, oxygen storage capability, and high ion conductivity, ceria (CeO_2) is a popular material in chemical catalysis [33–36] and solid oxide fuel cells (SOFCs) [37–39]. CeO_2 -based oxides can be used in three-way catalysts for the conversion of toxic gases in automobile exhaust [40]. As a reducible oxide, the surface oxygen atoms can be easily released to form O vacancies. The O vacancies at the surface of CeO_2 are believed to enhance the stability, dispersion, and catalytic activity of supported metals [41–43]. To increase the oxygen vacancy formation and catalytic properties of CeO_2 , generally two approaches have been explored. One is the development of a solid solution with other oxides such as ZrO_2 [33]. The oxygen vacancy formation energy was found to be lower in CeO_2 - ZrO_2 , which is possibly due to the lattice strain induced by incorporating Zr atoms [44,45]. For the substitution of some other metals such as Mn, Pr, and Sn, the decrease of vacancy formation energy is due to both electronic modification and structural distortion [46]. The other approach is to synthesize metastable CeO_2 nanoparticles with high energy facets. DFT studies have shown that the vacancy formation energy is lower on the (100) and (110) surfaces than on the (111) surface. It has been demonstrated that CeO_2 nanocubes with predominately {100} facets exposed are more active than CeO_2 nanooctahedra with primarily {111} facets exposed for water gas shift (WGS) and CO oxidation [47]. The ease of O vacancy formation on the (100) surface originates from the surface stability. Atomic or electronic reconstructions usually occur to lower the surface free energy and stabilize the material. One of the possible ways is the formation of surface O vacancies.

The models of bulk and surface structures are shown in Figure 11. Tasker classified the surfaces of ionic crystals into three types purely based on electrostatic considerations [48]. (This is a useful first approach to understanding the surfaces of oxides, but since this assumes that only ions exist it can in some cases be misleading, and a better strategy is a bond valence approach [49].) The crystal with type I surface consists of valence neutral layers. Along the [110] direction, CeO_2 with a fluorite structure consists of repeating valence neutral CeO_2 layers, as shown in Figure 11(B). The bulk terminated CeO_2 (110)

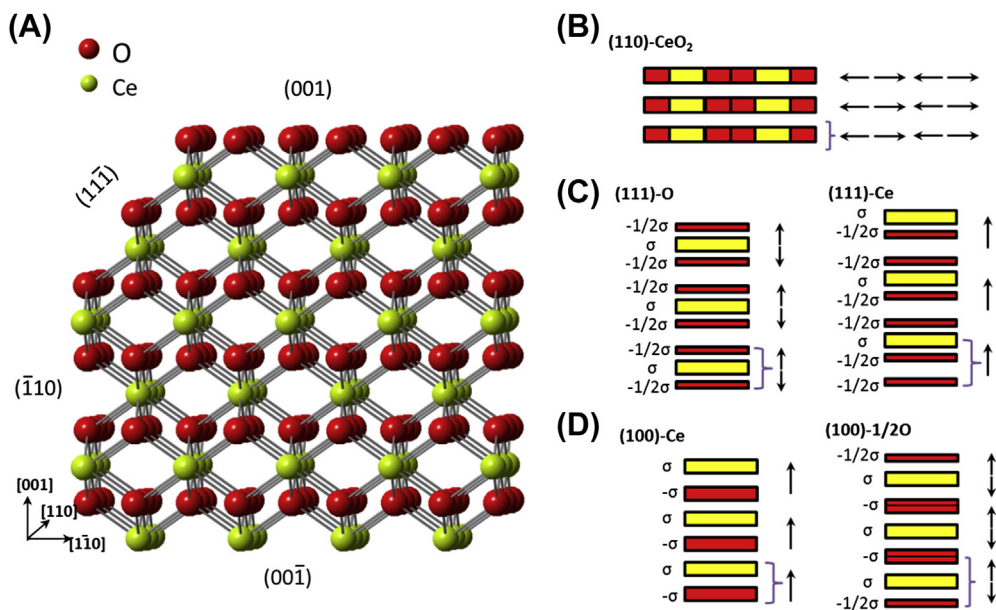


Figure 11 Schematic drawings of CeO_2 bulk structure (fluorite), surface structures, and associated dipole moments. (A) A CeO_2 structural model with truncated $\{100\}$, $\{110\}$, and $\{111\}$ surfaces. (B) Schematic view of the stacking of dipole moments along the $[110]$ direction. The red (black in print versions) and yellow (gray in print versions) boxes represent O and Ce atoms and each arrow represents a dipole moment. The curly brackets represent a repeating unit. (C) Schematic view of the stacking of dipole moments along the $[111]$ direction. The O-terminated (left) and Ce-terminated (111) (right) surfaces result in nonpolar and polar surfaces, respectively. (D) Schematic view of the stacking of dipole moments along the $[100]$ direction. The Ce-terminated (100) is a type III polar surface (left). The dipole moment can be compensated by transferring $\frac{1}{2}\text{O}$ atoms from an O-terminated side to a Ce-terminated side (right).

is a type I surface and is considered to be stable in most gas environments. The type II surface comprises repeating units of a tri-layer system in which the dipole moments are in opposite directions and cancel each other out. The type III surface consists of a stacking of repeated bilayers. Each repeating unit is associated with a dipole moment. The net dipole moment stacks up as the thickness increases and the resulting surface is polar and unstable except under highly reducing or oxidizing conditions. The CeO_2 (111) surface can be a type II or type III surface depending on the cation or anion surface termination. If the (111) surface is O terminated, the repeating unit is a sandwich-like $\text{O}^{2-}-\text{Ce}^{4+}-\text{O}^{2-}$ along the $[111]$ direction, as shown in Figure 11(C). In each repeating unit, the dipole moments with opposite directions cancel each other out. Therefore, the net dipole moment of each repeating unit is zero and the O-terminated CeO_2 (111) is a type II stable surface for most gas environments. If the (111) surface is Ce terminated, the (111) surface is then a type III unstable polar surface, as shown in Figure 11(C). In this case, the repeating unit in the $[111]$ direction should be chosen as $\text{Ce}^{4+}-\text{O}^{2-}-\text{O}^{2-}$. The net dipole

moments from each unit stack up and the electrostatic energy of the crystal diverges as the thickness increases. Therefore, the Ce-terminated CeO_2 (111) is expected to have high surface energy and the O-terminated CeO_2 (111) is energetically preferred.

The (100) surface is classified as a “type-III” polar surface. This type of surface is unstable in most cases and surface reconstructions or other stabilization mechanisms are expected to take place. Along the [100] direction, CeO_2 consists of repeating units containing a Ce^{4+} and a O^{2-} plane, as shown in Figure 11(D). For a stoichiometric CeO_2 nanocube (i.e., Ce and O layers on the opposite sides), a total dipole moment perpendicular to the (100) surface is induced. The macroscopic dipole moment can be quenched if the Ce-side surface is less positive and O-side surface is less negative by a factor of $\frac{1}{2}$. This value can be calculated based on the spacing between the cation and anion planes [50,51]. The most often assumed surface termination of CeO_2 (100) is O termination with half of the oxygen atoms removed on both sides. In this case, $\frac{1}{2}\text{O}^{2-}-\text{Ce}-\frac{1}{2}\text{O}^{2-}$ can be chosen as the repeating unit, as shown in Figure 11(D). The net dipole moment in each unit is zero and the surfaces become type-II nonpolar surfaces. For completeness, we will mention that under highly oxidizing conditions both the (100) and $(\bar{1}00)$ could be oxygen terminated; similarly Ce terminated under highly reducing conditions. However, the relatively large oxidizing or reducing conditions required for this will rarely be encountered in practice.

CeO_2 nanocubes have the {100} facet predominantly exposed, but the edges and corners are truncated by {111} and {110} surfaces, as shown in Figure 12(A). The surface structures of the three facets can be imaged simultaneously when the nanocube is tilted to the [110] zone axis, as shown in Figure 12(B). The Cc and Cs corrected HREM study performed by our group shows that the {111} surface is O terminated [13], which agrees well with electrostatic arguments. The experimental HREM image is shown in Figure 12(D) with the simulated image overlaid. Although the bulk terminated (110) surface is considered a stable surface, HREM experiments show that the (110) surface consists of (111) nanofacets and flat CeO_{2-x} layers. The simulated images with the Ce terminated (110) surface are shown in Figure 12(C). DFT studies indicate that the (111) surface has a smaller surface energy than the (110) surface. Thus (111) faceting is energetically plausible. However, inducing additional oxygen vacancies will eliminate the (111) nanofacets. Crozier et al. performed an environmental HREM study and showed that the (110) surface, which initially contains sawtooth-like features, becomes flat after annealing the nanoparticles at 600 °C in 0.5 Torr H_2 [52].

In contrast to the well-ordered reconstruction with $\frac{1}{2}\text{O}$ removed, the (100) surface appears to have multiple terminations [13]. Figure 12(E) and (F) are the experimental images of the top and bottom (100) surfaces. The two surfaces show the coexistence of O and Ce terminations. In Figure 12(E), the left part shows a Ce layer termination while the right part is O terminated. The structure with $\frac{1}{2}\text{O}$ removed seems to exist, as shown in region I of Figure 12(F), but it is not present over extended regions. Instead, the (100)

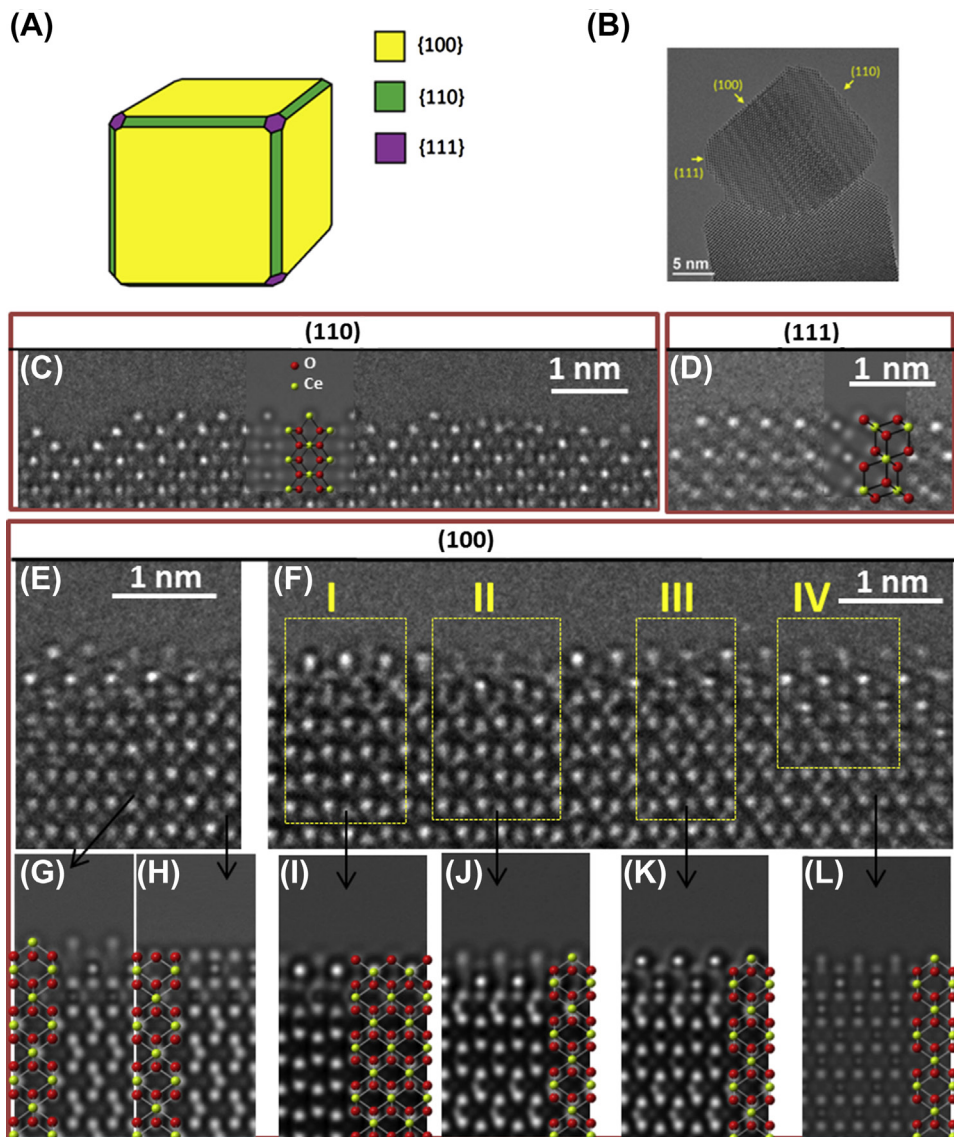


Figure 12 High resolution electron microscopy (HREM) studies of CeO_2 nanocubes. (A) A schematic drawing of the general shape of CeO_2 nanocubes. The $\{111\}$ and $\{100\}$ surfaces present on the edges of CeO_2 nanocubes with the $\{100\}$ surface predominantly exposed. (B) A transmission electron microscopy image of a CeO_2 nanocube viewing in $[110]$ direction. The (100) , (111) , and (110) facets can be observed simultaneously. (C) Experimental and simulated HREM profile-view images of CeO_2 (110) surfaces. The atom model is directly overlaid on the simulated image. (D) Experimental and simulated HREM profile-view images of CeO_2 (111) surfaces. (E), (F) Experimental HREM profile-view images of the (100) and $(\bar{1}00)$ facets. (G)–(L) Simulated HREM images of each area in the experimental images as indicated by the arrows.

surface contains a large number of cation and anion vacancies, which is evidenced by the significant contrast difference of the surface and bulk Ce atoms in the HREM image. As the thickness increases, the Ce columns become black spots while the O columns maintain white contrast. However, at the near-surface in regions I–III, both Ce and O atoms show white contrast. This is mainly due to the low occupancies of atoms at the surface region. The low occupancy lowers the average density of the atoms, and thus the intensity oscillation is slower compared to the fully occupied regions. The atom positions in the surface area (~ 1 nm) are partially occupied, which implies the presence of Ce and O vacancies. In addition, the vacancy concentrations are inhomogeneous on the surface, as the contrast of both surface Ce and O atoms changes randomly. DFT studies show that the formation of O vacancies is accompanied by the reduction of neighboring Ce^{4+} to Ce^{3+} [53], as expected from valence arguments, and this reduction was observed in the near surface region (>1 nm) in EELS studies [54,55]. Therefore, (100) surfaces of as-prepared CeO_2 nanocubes contain reasonable concentrations of Ce and O vacancies. The outermost surface can be terminated by Ce, O, or reconstructed CeO. The TEM characterization is in agreement with FT-IR studies [56] using methanol adsorption on CeO_2 nanocubes, nanorods (primarily $\{110\}$ and $\{100\}$ facets exposed), and nanooctahedra (predominantly $\{111\}$ facets exposed). Only on-top methoxy adsorption was observed on the nanooctahedra. In contrast, on-top and several bridging adsorptions were found on CeO_2 nanocubes and nanorods. The IR studies imply the (100) surface consists of a large amount of disordered O vacancies as well as some amount of Ce termination.

Clearly the stabilization mechanisms affect the surface structures of CeO_2 . However, the surfaces are not solely dependent on electrostatic effects. For the nonpolar (110) surfaces, (111) faceting can further reduce the surface energy. For the polar (100) surface, a reduced surface region with multiple surface terminations is present instead of a single well-ordered surface termination. In this case, strictly speaking, the (100) surface is not a well-defined surface, which helps to compensate the dipole moment. The formation of the “partially disordered” (100) surface is possibly due to the relatively small energy difference between the different orderings of surface O vacancies. It is also possible that the ordering of O vacancies is related to O partial pressures. The phase diagram of the Ce–O binary system shows a variety of intermediate CeO_{2-x} ($x \leq 0.5$) structures with respect to O partial pressure [57]. The reduction process typically starts at the surface owing to the reducing environment. With diffusion of the O atoms to the surface, the O vacancies diffuse into the crystal simultaneously [58]. A certain type of O vacancy ordering is energetically preferred if the surface is reduced to a certain extent. Indeed, well-ordered surface reconstructions are resolved by STM studies on single crystal CeO_2 at elevated temperatures under UHV conditions [59] (highly reducing). It is worth noting that CeO_2 has a centrosymmetric fluorite structure, hence having similar features on the two opposite surfaces (e.g., the (001) and $(\bar{1}00)$ surfaces) is reasonable. For the polar surfaces

of some non-centrosymmetric material, the chemistry of two opposite surfaces can be different. For example, the ZnO (0001)-Zn and $(000\bar{1})$ -O surfaces possess distinct structures according to DFT and STM studies [60].

Although HREM profile-view imaging can show occupancies of atom columns, it is not sensitive to 2D defect surface structures. Further detailed atomic structures can be obtained with the help of single crystal studies on CeO₂ surfaces, particularly for the (111) surface. For example, Esch et al. used DFT and STM studies to show that subsurface oxygen vacancies are critical for the formation of linear vacancy clusters on the (111) surface [61]. The study indicates that subsurface vacancies can enhance further surface oxygen release in catalytic applications. Here the subsurface refers to the third surface layer (O layer). Recently a (2×2) ordering of subsurface O vacancies was reported by Torbrügge et al. using AFM [62], which is also in agreement with later STM and DFT studies [63,64]. The structural characterization of the surfaces of nanoparticles and single crystals using different techniques can provide us with a more comprehensive understanding.

4.1.2 SrTiO₃ Nanocuboids

SrTiO₃ has a wide range of applications from thin film growth [65–67] to catalysis [68]. Recently it was discovered that SrTiO₃-based catalysts have high catalytic activity in soot combustion [69]. The synthesis of well-defined SrTiO₃ nanocuboids has provided new catalytic insights that are unobtainable from standard bulk SrTiO₃ [70–72]. The nanocuboids have the {100} facet exposed, which is close to a thermodynamically stable Wulff shape but more accurately is a growth shape (kinetic Wulff shape, e.g., [73] and references therein). As SrTiO₃ has a lattice constant of 3.905 Å, which is very close to the lattice parameters of Pt and some other metals, epitaxial growth of these metals on SrTiO₃ nanocuboid supports is expected. The stable support and good epitaxy between the support and metal can improve the stability of catalysts [74].

The surface structures of SrTiO₃ single crystals are rather complex and have been extensively investigated. SrTiO₃ has a standard perovskite structure consisting of a repeated stacking of strontium oxide (SrO) layers and titanium dioxide (TiO₂) layers in the [100] direction, as shown in Figure 13. If a SrTiO₃ surface is truncated in the [100] direction, the question of simple surface termination inevitably arises: Is the (100) surface terminated with SrO or TiO₂? In principle, the SrO and TiO₂ terminations can coexist for a vacuum-cleaved surface. A variety of surface reconstructions other than the SrO and TiO₂ terminations were observed after high temperature annealing (typically >800 °C). A number of surface reconstructions have also been reported on SrTiO₃ (100) single crystals prepared under different conditions [75–83]. Among them, the well-ordered (2×1) [75], c(4×2) [81], and (2×2) [84] surface reconstructions have been structurally solved by using a variety of techniques and there are additional, plausible structures such as locally ordered (3×3), ($\sqrt{5}\times\sqrt{5}$) R26.6° and ($\sqrt{13}\times\sqrt{13}$) R37.7°

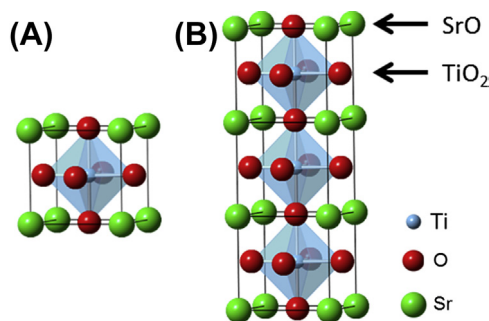


Figure 13 Bulk and surface structures of SrTiO_3 . (A) Schematic view of a SrTiO_3 unit cell. (B) Illustration of two possible bulk truncations of SrTiO_3 (100): SrO and TiO_2 surface terminations.

surfaces [85]. Interestingly, all of the reconstructions have TiO_2 double-layer termination features, in which both the surface and subsurface are TiO_2 layers. The TiO_2 -rich (100) surface can be obtained by etching a single crystal in a buffered NH_4F – HF solution [86], which is a standard technique in thin film processing. This is probably due the greater basicity of surface SrO compared to the TiO_2 layer. Prolonged annealing can also result in a variety of surface features such as islands [87], step-terrace structures [88,89], ridges [90], and canyon-like features [91]. The non-flat morphological features can either be Sr-rich or Ti-rich depending on the O partial pressure during annealing [92–94], which suggests that O and Sr vacancies may play an important role in the surface chemistry of SrTiO_3 .

However, most of the reconstructed surface structures on SrTiO_3 single crystals are obtained after high-temperature annealing. The sample preparation is very different from the SrTiO_3 nanocuboid growth condition or catalytic reaction environments. The temperatures for some wet syntheses of SrTiO_3 nanocuboids are around 200°C . Some surface reconstructions may not yet be activated in these conditions owing to the low temperature, as the formation of some stable reconstructions requires the overcoming of energy barriers. In addition to the temperature difference, solution-based synthesis involves the addition of different precursors with or without organic ligands. Whether or not the surface structures of SrTiO_3 single crystals are the same as the nanocrystals is a question of interest. Additionally, the impact of synthetic method on nanocuboid surface structure is an intriguing research topic.

To address these problems, our group studied the surface structures of SrTiO_3 nanocuboids prepared by three different hydrothermal syntheses. The first type of synthesis uses oleic acid as a capping agent as proposed by Hu et al. [72]. The end products are nanocuboids with a size of ~ 20 nm. The second hydrothermal route does not use oleic acid and results in nanocuboids with a size of ~ 65 nm [70]. During this synthesis, acetic acid was used to dissolve the $\text{Sr}(\text{OH})_2$, which was used as the Sr precursor. The third method is the same as the second one but uses a microwave oven instead of a

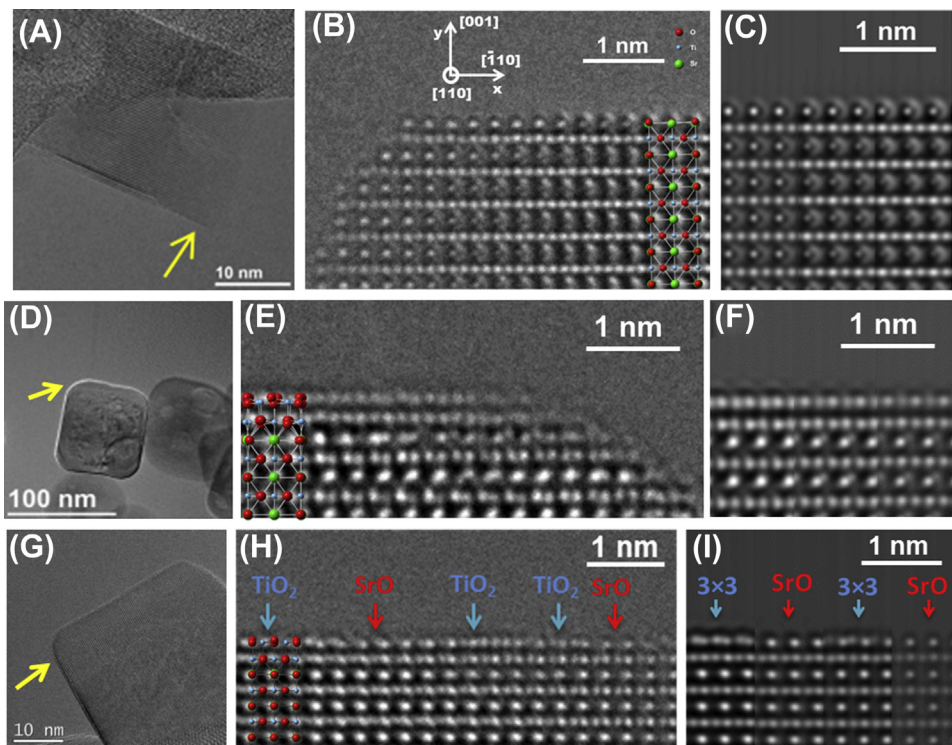


Figure 14 Comparison between the (100) surfaces of SrTiO₃ nanocuboids obtained by three hydrothermal processes. The atomic resolution surface structures are imaged by high resolution electron microscopy (HREM) profile-view studies. (A)–(C) Low magnification transmission electron microscopy, experimental HREM, and simulated HREM images of the SrTiO₃ (100) surface prepared by oleic acid synthesis. (D)–(F) Low magnification, experimental HREM, and simulated HREM images of the SrTiO₃ (100) surface prepared by acetic acid synthesis. (G)–(I) Low magnification, experimental HREM, and simulated HREM images of the SrTiO₃ (100) surface prepared by microwave synthesis.

conventional oven [14]. The apparent “benefit” of microwave synthesis is that it significantly reduces the hydrothermal treatment time from ~20 h to ~20 min. The microwave synthesis results in nanocuboids with a size of ~35 nm. Typical TEM images are shown in Figure 14 to demonstrate the general shapes of SrTiO₃ nanocuboids obtained by different preparation methods. The three methods will be referred to as oleic acid synthesis, acetic acid synthesis, and microwave synthesis, respectively.

The atomic surface structures of the nanocuboids obtained by the three different methods are obviously different, as shown in Figure 14. The nanocuboids obtained by oleic acid synthesis are SrO terminated. Figure 14(B) shows an experimental HREM image along the [110] viewing direction. The simulated HREM image using a SrO terminated surface matches with the experimental image well, as shown in Figure 14(C). In addition, HREM simulation reveals that some of reconstructed surface structures

show (1×1) periodicity along the $[110]$ zone axis. The simulated surface contrast is significantly different from the experiment [14]. The simulated image of the SrO surface matches the experimental image best among the tested structures. The acetic acid synthesis results in a double-TiO₂ layer reconstructed surface, as shown in Figure 14(E). The simulated HREM images using the locally ordered $(\sqrt{13} \times \sqrt{13})$ R37.7°, $(\sqrt{2} \times \sqrt{2})$ R45°, and $(\sqrt{5} \times \sqrt{5})$ R26.6° surface structures match better than the other surface reconstructions. As the difference between the three locally ordered reconstructions is small, it is possible that these structures can coexist on the nanocuboids. A simulated HREM image using a $(\sqrt{13} \times \sqrt{13})$ R37.7° surface model is shown in Figure 14(F). Interestingly the microwave synthesis not only reduces the required time of hydrothermal treatment, but also changes the atomic surface structures, as shown in Figure 14(H). The surface has a mixed termination of both double-TiO₂ layer reconstructions and SrO terminations. The simulated HREM image is shown in Figure 14(I), in which the (3×3) reconstruction [85] was used to simulate the double-TiO₂ layer feature in the experiment.

The presence of the SrO termination on the as-prepared nanoparticles is attributed to the capping oleate from the oleic acid synthesis. Hu et al. carried out in situ SAXS and WAXS and found that a lamellar microemulsion was formed during the hydrothermal synthesis [72]. The oleic acid in the microemulsion confines the nanocuboids and limits their size. The end products are nanocuboids with surfaces covered by a layer of oleate, which was confirmed by FT-IR studies [14]. As the oleic acid is expected to bond preferentially with the more basic SrO termination, the relatively unstable SrO-terminated surface is protected by the oleate molecules. For the acetic acid synthesis, no organic ligands are present, and the surface structures should be mostly controlled by thermodynamics, with the lowest energy structure dominating. The observed surface reconstructions are consistent with DFT predictions under vacuum conditions. The $(\sqrt{13} \times \sqrt{13})$ R37.7°, $(\sqrt{2} \times \sqrt{2})$ R45°, and $(\sqrt{5} \times \sqrt{5})$ R26.6° surface structures are located in the energy convex hull [85]. The microwave synthesis is a relatively new technique and its complete influence on the synthesis is not yet well understood. The effect of the microwave synthesis on the surface structure can either be simply due to the shorter reaction time or more complex mechanisms. More future studies are required for a comprehensive understanding.

The effects of ligands on the properties of catalysts have been reported in the past. Mostly the ligand was assumed to block reactant access to the catalyst surface [95,96] or affect the electronic structure of catalyst [97–100]. This study shows that the atomic surface structures of mixed metal oxides may in fact be changed by the ligands. The results may be extended to other similar materials, particularly for mixed metal oxides with different surface acidities. In addition, the SrO- and TiO₂-rich surfaces can result in the morphological change of the supported Pt particles [101]. It has been demonstrated that the oxygen reduction reaction (ORR, O₂ to H₂O and O₂ to H₂O₂) is

sensitive to the shape of Pt on SrTiO₃ substrates [102]. And for some reactions, the selectivity can be tuned by the facets of Pt [103]. In these studies, either Pt single crystals or relatively large Pt nanoparticles are used. Controlling the morphology of Pt through controlling the atomic surface structures of the supports may be a more viable method in catalytic applications.

4.2 Surface Relaxations: Adsorbate Induced or Intrinsic

In aberration-corrected HREM or STEM images, picometer precision can be achieved [12,104]. At such a level of precision, small surface relaxations can be clearly imaged. Lattice relaxation typically happens at the low-coordinate atoms except for those on very close-packed surfaces. Together with DFT calculations, the measurement of surface relaxations by HREM or STEM can provide additional information about the surface atomic and electronic structures of catalysts. However, the relaxation measurements should be carefully conducted as the exact peak positions of the spots are not necessarily the real atom positions. The peak positions can deviate from the real atom positions due to residual aberrations, specimen tilt, or even the intrinsic phenomena of the electron-specimen interaction (in the case when column approximation does not hold). In STEM imaging, the scanning noise can also cause mismatch between the spot and atom positions. Performing DFT calculations and quantitative image simulations can identify whether the surface relaxations are real or simply the effects of HREM/STEM imaging.

Our group investigated the surface relaxation of SrTiO₃ nanocuboids with a SrO termination [14]. The surface layer has an inward contraction while the second surface layer has an outward expansion. The interlayer spacing measured from the experimental image was compared to the measurement from simulated HREM images with DFT relaxed surface structures. The experimental surface relaxation matches with the DFT results well, which implies a clean SrO-terminated surface without adsorption. Interestingly the lattice spacing shows oscillations of ~50 pm in the bulk region while in principle these should not exist, as the interlayer spacing between the SrO and TiO₂ layers should be the same if there is no relaxation. This implies that the spot peak positions in an HREM image are not always the exact atom positions. We found that residual aberrations and specimen tilt cause deviation of the peak positions from the exact atom column positions. More specifically, the peak intensity of the Ti column is higher than the SrO column at a certain imaging condition. A distortion of the HREM image will distort the low intensity spots (SrO) more than the high intensity spots (Ti). As a result, the distances between the alternating Ti and SrO peak positions appear to oscillate.

As one example, surface relaxation measurements were conducted by Yu et al. in studying the (111) surface of Co₃O₄ nanocubes using aberration-corrected HREM (Figure 15) [12]. Co₃O₄ has attracted great interest for its applications in lithium battery [105,106] and catalysis [107–110]. It has shown that the Co₃O₄ nanorods

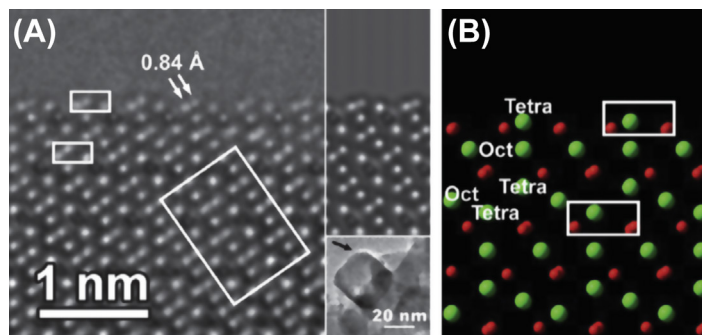


Figure 15 The (111) surface of Co_3O_4 nanocubes. (A) High resolution electron microscopy (HREM) profile-view image shows the (111) surface is terminated by the tetragonal Co atoms. The simulated HREM image is shown in the right side with the low magnification transmission electron microscopy image shown on the lower right corner. (B) The structural model of tetragonal Co-terminated (111) Co_3O_4 surface. Reprinted figure with permission from Yu et al. *Phys. Rev. Lett.* 105 226101 (2010). Copyright (2010) by the American Physical Society.

have high activity for CO oxidation even at $-77\text{ }^\circ\text{C}$ [109]. Co_3O_4 has a spinel structure with the AB_2O_4 general formula. For Co_3O_4 , A and B are, respectively, the tetrahedral and octahedral sites of Co. Along the [111] direction, the sequential stacking of B3-O4-A-B-A-O4 results in six possible terminations of the (111) surface. Yu et al. performed aberration-corrected HREM and found that the (111) surface of Co_3O_4 is a tetrahedral Co layer (Co^{2+}) with an O layer as the subsurface. Beyond the surface termination determination, the lattice spacing measurement shows a significant inward relaxation ($\sim 0.35\text{ \AA}$) of the outmost surface and a moderate inward relaxation ($\sim 0.1\text{ \AA}$) of the subsurface. The relaxations of the first three layers of the (111) surface measured from HREM images match well with the surface relaxations predicted by DFT calculations. Based on electrostatic arguments, the (111) surface is a polar surface. The surface Co^{2+} should be more positive in order to compensate for the surface polarity. As only a stoichiometric and clean (111) surface were considered in the DFT calculations, a good match of DFT and experiment measurement of surface relaxation can almost rule out the possibility of surface polarity compensation by adsorbing charged external species. The authors assigned the polarity compensation to the electron redistribution associated with surface relaxation, which was further supported by their calculation of the Bader charge of surface O and Co.

4.3 Supported Metal Nanoparticles

Supported metal catalysts are used in many catalytic reactions. Catalytic supports can improve the dispersion and stability of the metal. In addition, many studies have demonstrated that supports can have strong interaction with the metal, which can significantly

affect reactivity and selectivity. Designing a supported metal system with high activity, selectivity, and stability is of great interest in heterogeneous catalysis.

4.3.1 The Equilibrium Shapes of Freestanding and Supported Metal Particles

Under thermodynamic considerations, the equilibrium shape of a freestanding metal particle can be derived from the Wulff construction. The exposed facets of metal particles are typically the low-index surfaces with relatively small surface free energies (the surface energy per unit area). The distance from the center of the particle to an exposed facet (h_{hkl}) is proportional to the surface free energy (γ_{hkl}) of that facet, which can be expressed as:

$$\gamma_{hkl}/h_{hkl} = \text{const.} \quad (1)$$

Therefore the smaller the surface free energy is for a given facet, the larger the exposed area is for that facet. The calculated Wulff shapes of some popular catalytic metals can be found in Ref. [111]. The close-packed surfaces usually have low surface free energies, and they are therefore predominately exposed for equilibrium shapes. Examples are the (111) surface for fcc metals and the (110) surface for bcc metals. For a Pt particle, the Wulff shape is a truncated octahedron with {111} and {100} facets exposed, as shown in Figure 16(A).

If the freestanding metal is synthesized on a substrate, the interface should be accounted for in the shape determination. Qualitatively we can expect an orientation of the metal particle on the support should create a low energy interface. In materials science, low energy grain boundaries usually have a high lattice match (coincidence sites), which is why the epitaxial growth in a specific direction is usually favored. The total system energy can be further reduced by tuning the ratio of surface and interface areas. It is expected that a metal layer will completely wet the surface of the substrate or even form a solid solution with the substrate if the metal-substrate interface is extremely favorable. An energetically unfavorable interface has a strong driving force to minimize the interfacial contact, in which case the metal particles are very hard to grow on the substrate and forming freestanding particle is favorable. A more detailed investigation of supported metal shapes was developed by Kaichew [112] and Winterbottom [113]. According to the Winterbottom shape, the wetting of the metal particle on the substrate is determined by the energy of the interface as well as the energies of the surfaces of substrate and metal particles. The interfacial free energy (γ_{int}) is defined as:

$$\gamma_{\text{int}} = \gamma_{\text{metal}} + \gamma_{\text{substrate}} - \gamma_{\text{bond}} \quad (2)$$

where γ_{metal} is the surface free energy of the metal, $\gamma_{\text{substrate}}$ is the free energy of the substrate, and γ_{bond} is the free energy due to the bonding of the metal and substrate. If $\gamma_{\text{int}} - \gamma_{\text{substrate}} = 0$, exactly half of the metal will be exposed. Otherwise the exposed metal shape will deviate from the half Wulff shape. With an increase in interface energy, the

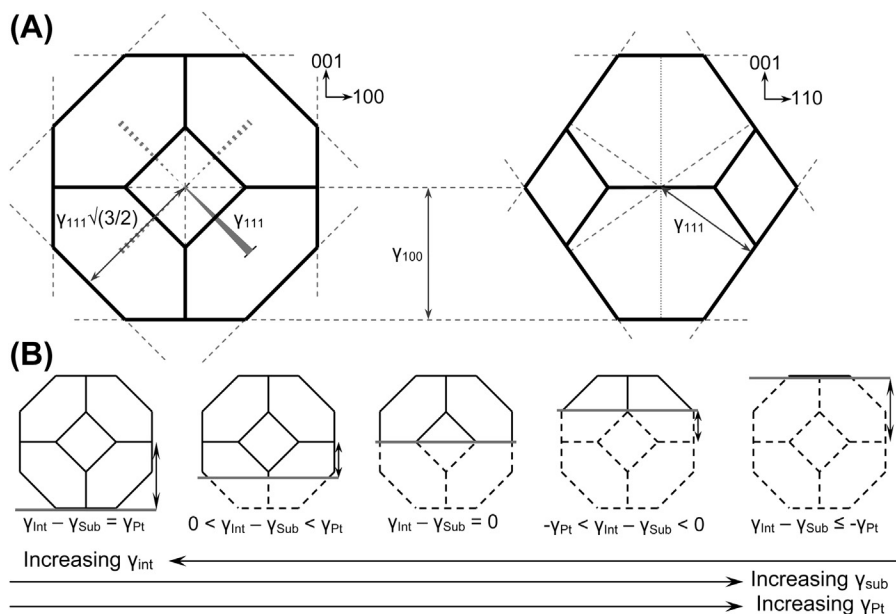


Figure 16 Equilibrium shapes of freestanding and supported Pt particles. (A) Equilibrium shape of a freestanding Pt particle using the $\gamma\{111\}:\gamma\{100\}$ ratio of 0.84 from Vitos et al. [111] (B) The Winterbottom shape of Pt particles on supports with different interfacial and surface energies. A strong bonding between Pt and substrate results in larger extent of wetting. Reprinted with permission from Enterkin et al. *Nano Lett.* 11 (2011) 993–997. Copyright (2011) by the American Chemical Society.

exposed area of the Wulff shape can increase up to the limit of a “fully” exposed metal particle ($\gamma_{\text{int}} - \gamma_{\text{substrate}} = \gamma_{\text{metal}}$). For the opposite scenario in which $\gamma_{\text{int}} - \gamma_{\text{substrate}} \leq -\gamma_{\text{metal}}$, the substrate will be completely wetted by the metal and no Wulff shape will be exposed. Figure 16(B) shows the Winterbottom shape of Pt with the change of interfacial energy.

Therefore, the shape of metal catalyst can be controlled thermodynamically if the substrate is homogeneous. Enterkin et al. demonstrated an example of the equilibrium Pt metal shapes on SrTiO_3 nanocuboids, which have the $\{100\}$ surface primarily exposed [114]. The Pt metal particles were synthesized on the SrTiO_3 nanocuboids by atomic layer deposition (ALD). The SrTiO_3 nanocuboids were prepared by the acetic acid synthesis [70], which resulted in TiO_2 -rich surfaces, as described in the previous section. SrTiO_3 has a lattice parameter 3.905 Å which is very close to that of Pt (3.920 Å). Previous experimental and theoretical studies show that there is a low energy interface between Pt (100) and SrTiO_3 (100) surfaces [101]. As a result, epitaxial growth occurs in the [100] direction (cube-on-cube). DFT calculations show that the TiO_2 -rich SrTiO_3 surface has a surface free energy similar to the $\{100\}$ surface of Pt. Therefore the expected shape of Pt particles deposited on SrTiO_3 nanocuboids is close to a half Wulff shape with a cube-on-cube epitaxial direction. This expectation was confirmed by the HREM study, as shown in Figure 17.

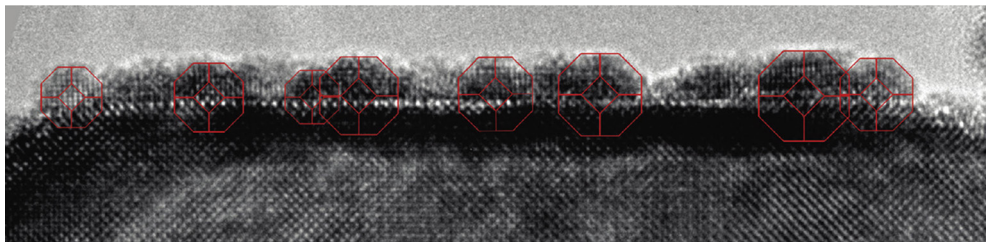


Figure 17 An high resolution electron microscopy image demonstrating the shape and interfacial structures of Pt grown on SrTiO₃ nanocuboids by atomic layer deposition. *Reprinted with permission from Enterkin et al. Nano Lett. 11 (2011) 993–997. Copyright (2011) by the American Chemical Society.*

By having a stable metal–support interface as well as equilibrium metal shapes, the sintering probability of the metal particles is reduced. Hence the stability of catalysts during catalytic cycles can be improved. A study of propane oxidation shows that the Pt–SrTiO₃ system has better stability compared to the Pt– γ -Al₂O₃ system [74]. It is also possible that by tuning the lattice parameter of the substrate, the wetting of the metals on the support can be controlled. For the SrTiO₃ case, this can be achieved by substituting Ba for Sr (for BaTiO₃ $a = b = 3.992 \text{ \AA}$, $c = 4.036 \text{ \AA}$), which changes the lattice parameters slightly and can therefore alter the ratios of exposed Pt {100} and {111} facets [115]. As Pt {111} and {100} facets are known to have different selectivities for some reactions [103], it is possible to control the catalysis in a thermodynamic way [115].

4.3.2 The Shapes of Supported Metal Catalysts under Reaction Conditions

The DFT calculated energies are for the ground state configuration, and are often for clean surfaces. It is possible that the equilibrium shape or interface structure changes during the catalytic reaction. This is primarily due to chemisorption on the particle or a change of the interface between the particle and support. The changes usually depend on specific gases and catalytic systems. In this review, we focus on some experimental studies to obtain insight into reaction-induced morphological changes. The dynamic process can be imaged by ETEM.

Hansen et al. provided clear evidence of shape changes in supported copper nanocrystals using ETEM [116]. The authors conducted a comparative study on the shapes of Cu nanoparticles supported on ZnO and SiO₂ under different gas environments at 220 °C. They observed shape changes of Cu particles after adding H₂O to pure H₂ on both the ZnO and SiO₂ supports. They also demonstrated that the shape change can be reversed by removing the H₂O gas from the systems. Thus the authors deduced that H₂O is adsorbed on the Cu surface and induces the shape change. In contrast, if CO was added to the pure H₂ environment instead of H₂O, a shape change was only observed on the ZnO-supported Cu. This indicates that the shape change is due to the reduction of the Cu–ZnO interface by CO. Therefore, both metal surfaces and the metal–support interfaces can be affected by the surrounding gases.

Systematic studies of the dynamic behavior of supported particles provide insights into their catalytic properties. Several elegant ETEM experiments have been performed to understand the reaction mechanism for CO oxidation on supported Au nanoparticles (GNPs) [10,117–119]. Au shows remarkable catalytic activity for CO oxidation even at room temperature. Unlike other metal catalysts, such as Pt, Pd, and Ru, bulk Au is almost completely inert to chemisorption [120–122], and adsorption is essential for the surface reactions on catalysts. The high activity of CO oxidation was initially found on oxide supported GNPs [123], and triggered extensive studies and considerable debates [124–126]. It is generally believed that the low-coordinated Au sites [127], the metal-support interaction [128], and quantum size effect for the small site (less than ~ 2 nm) [129] are responsible for the enhanced activities. By establishing a “safe” electron dose range in the ETEM so that electron-induced morphological changes of Au are minimized [117], Uchiyama et al. studied the shape changes of Au supported by CeO₂ and TiC in CO/air, N₂, O₂, and vacuum, as shown in Figure 18(A) and (B) [118]. No significant morphological change was observed for TiC-supported GNPs in different gas environments. On the other hand, CeO₂-supported GNPs became rounded upon exposure to O₂. As CeO₂-supported GNPs usually show much higher CO oxidation activities than TiC-supported GNPs, the distinct, morphological behaviors of the GNPs on two supports may be correlated to the catalytic processes. By increasing the CO/O ratio, the GNPs on CeO₂ supports become more faceted. An experimental shape diagram showing the effects of CO and O partial pressures on GNP shape is depicted in Figure 18(C). The adsorption of CO molecules on the GNP was believed to stabilize the polyhedral shape of GNPs. In our opinion, it is also possible that additional O vacancies were created under the reaction conditions. The O vacancies also help to stabilize the Au particles [41]. The dissociative adsorption of O₂ on the perimeter of the Au–CeO₂ interface may cause formation of rounded or multifaceted GNP surfaces. The understanding of the reaction mechanism was further developed by Ta et al. [43]. Their mass spectroscopy study showed that CO₂ was immediately produced when CeO₂-supported GNPs were exposed to pure CO at room temperature, which implies the lattice O of CeO₂ can participate in the CO oxidation. Note that for pure CeO₂, the conversion of CO typically starts at ~ 500 K [130]. If the isotopic ¹⁸O₂ was injected into the system, the mass spectra revealed the presence of C¹⁶O¹⁸O. This indicates that O dissociation is facilitated by CeO₂. The CeO₂-promoted dissociative adsorption of O species improves CO oxidation compared to the use of only Au particles.

Recently the mobility of CeO₂-supported GNPs was studied at atomic resolution by Kuwauchi et al. [10]. Using ETEM, it was observed that the GNPs are displacing and rotating back and forth between equivalent sites of the Au–CeO₂ (111) interface under 1 vol% CO/air. The frequency of this reversible motion is ~ 6.4 s⁻¹. In contrast, the frequency of this stepwise displacement is ~ 14.4 s⁻¹ in O₂ gas. The lower frequency was attributed to the oxygen vacancies created under these reaction conditions. Their DFT

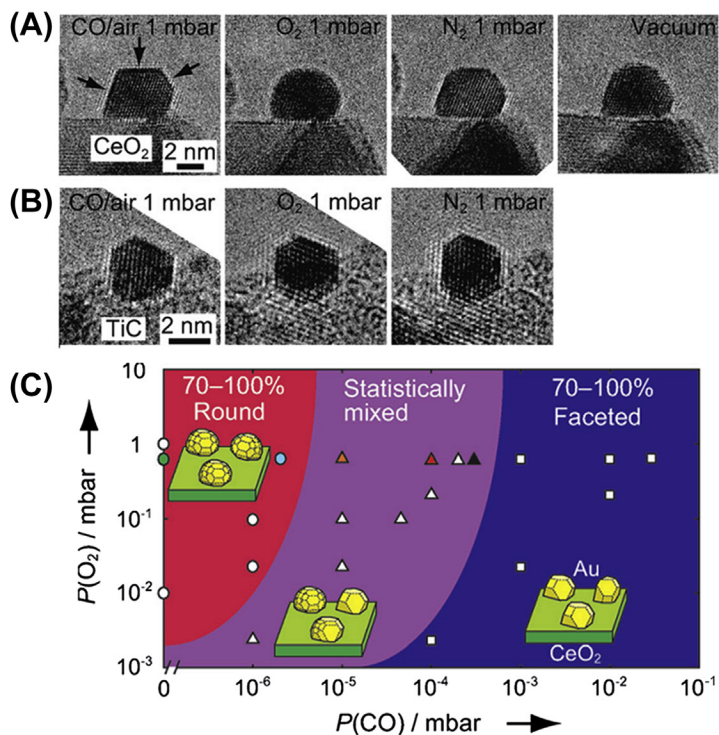


Figure 18 Shape of supported gold nanoparticles (GNPs) in vacuum and gaseous environments. (A) The shapes of GNPs on CeO₂ supports under different gases and vacuum conditions. (B) The shapes of GNPs on TiC supports in different gases. (C) A phase diagram showing the shapes of the CeO₂-supported GNPs versus the partial pressure of CO and O₂. Reprinted by permission from Uchiyama et al. *Angew. Chem. Int. Ed.* 50 (2011) 10157–10160, copyright (2011) Wiley-VCH Verlag GmbH & Co. KGaA, Weinheim.

study shows that the energy to displace GNPs on a Ce-terminated surface is much larger than for the O-terminated surface. Note that experimental studies show that the CeO₂ (111) surface is O terminated in both single crystals [131,132] and nanoparticles [13,55]. However studies show that linear O vacancies are present after annealing [61]. The result further confirms that the O vacancies on the CeO₂ (111) surface provide strong anchoring of the supported GNPs. The strong anchoring enhances the stability of the catalyst during reactions.

4.3.3 Other Thoughts: Manually Controlling the Shapes of Supported Metals

In the past decades, both metals and supports with well-defined shapes have been synthesized [133,134]. However, manual control of supported metal systems is relatively rare. Yamada et al. employed a Langmuir–Boldgett (LB) trough to physically pack the well-defined supports and metals to generate active interfaces for catalytic reactions [96].

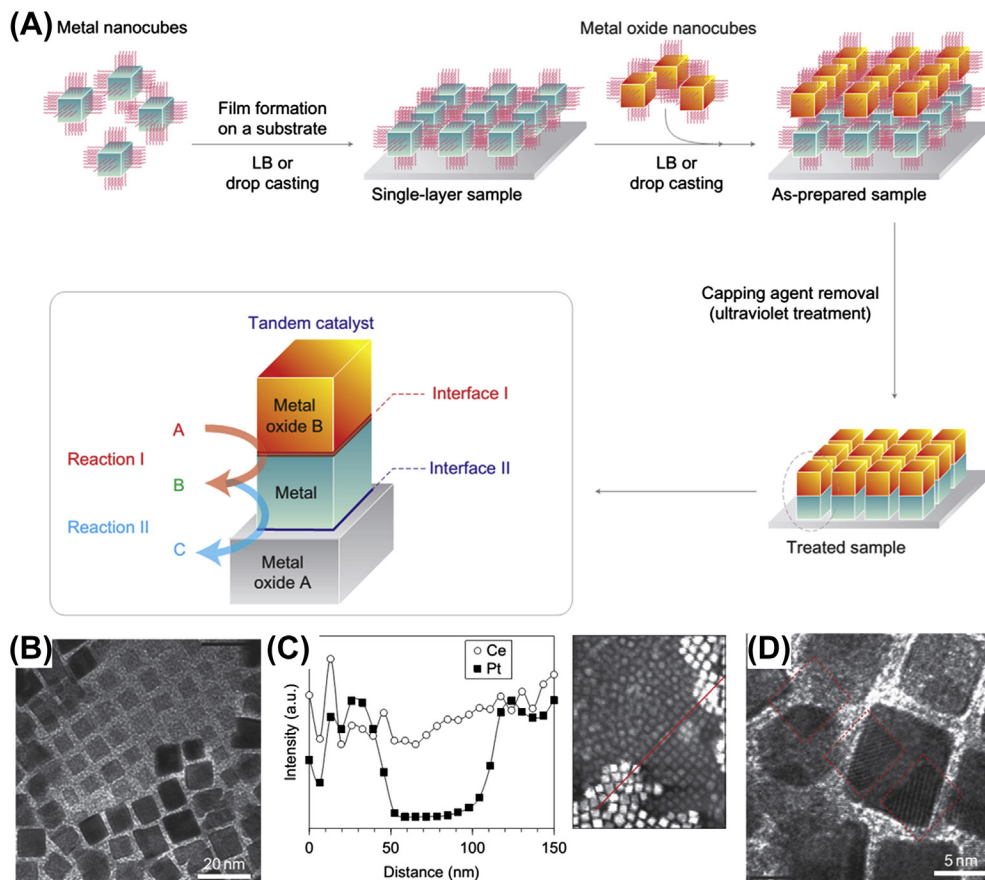


Figure 19 Design of a tandem catalyst system with two active interfaces for different reactions. (A) A schematic view of preparing a tandem catalyst. (B) A transmission electron microscopy image of a defect area of a bilayer film. (C) Energy dispersive X-ray spectroscopy line scan (left) along the defect area (right). (D) A high resolution electron microscopy image of a bilayer area with the Moiré pattern generated by the Pt and CeO₂ nanocubes. Reprinted by permission from Macmillan Publishers Ltd: Yamada et al. *Nat. Chem.* 3 (2011) 372–376, copyright 2011.

This may provide a possible method for developing well-defined supported metal catalysts. The LB trough may be utilized to deposit monolayers of amphiphiles of interest onto solid supports. These amphiphiles can include organic ligands often used in catalyst synthesis. Figure 19(A) shows the schematic of preparing the tandem catalyst systems using the LB approach. In their study, oleylamine-capped Pt nanocubes were dispersed in chloroform. The suspension was dropped into an LB trough with water as a subphase. After evaporating the chloroform, an LB thin film consisting of Pt nanocubes on the water surface was generated. The thin film was then transferred onto a Si wafer. A similar approach was used to generate a CeO₂ nanocube LB thin film. The thin film was

transferred to the as-prepared Si-Pt substrate. The residual capping agents which helped to uniformly separate the nanocubes were removed by ultraviolet treatment. The formation of active metal oxide interfaces was further confirmed based on changes observed in sum frequency generation vibrational spectroscopy and the apparent activation energy of CO oxidation. Thus a tandem catalyst containing CeO₂, Pt, and SiO₂ (as the surface of Si wafer is oxidized) was prepared with two active interfaces including SiO₂-Pt and CeO₂-Pt. The tandem morphology was confirmed by plan-view HREM and EDS. At the defect areas where the tandem system was not generated, the contrast difference is obvious, as shown in Figure 19(B). The EDS line-scan (Figure 19(C)) shows the difference in amount of Ce and Pt between the tandem and defect areas. In Figure 19(D), the HREM lattice fringes confirm the presence of CeO₂ and Pt, as well as the interfacial area according to the Moiré pattern.

The tandem catalyst system has multiple benefits. The CeO₂-Pt interface is active for the decomposition of methanol to CO and H₂, while the Pt-SiO₂ interface is able to catalyze olefin hydroformylation using CO and H₂. The tandem catalyst can thus be used to form propanal (ethylene hydroformylation) by in situ methanol decomposition. In contrast, the use of only Pt-SiO₂ catalysts to form propanal from CO and H₂ would cause the formation of methanol in addition to the propanal formation. The overall selectivity of propanal formation was more than 94%. The enhanced properties are probably due to the high concentration of methanol which reduces the rate of methanol formation, as well as the high concentrations of CO and H₂ which accelerate propanal formation.

This study indicates that synthesis techniques which are often used in other areas may be employed to geometrically control supported catalytic systems. The LB trough in this tandem catalyst synthesis as well as some other techniques such as ALD and electron lithography [102] may be used for the future design of functional catalytic systems. For example, ALD, which is widely used for layer-by-layer thin film growth, has been used for supported catalyst design to selectively coat oxide surfaces while leaving the metal particles exposed [135]. Owing to the coating design, coking and sintering under reaction conditions are significantly suppressed. On the other hand, electron microscopy helps to verify if the expected configurations have been realized.

4.4 Bimetallic Catalysts

Bimetallic systems have attracted great interest in heterogeneous catalysis over the past few decades. The advantages of using bimetallic catalysts have been demonstrated over a variety of reactions such as catalytic reforming [136,137], oxygen reduction reaction (ORR, in cathode of fuel cell, O₂ to O⁻ and O²⁻) [138,139], preferential CO oxidation in excess hydrogen (PROX) (by CO + ½O₂ → CO₂ in excess H₂) [140–142], and hydrodesulfurization [143]. Incorporating another metal species into the parent metal can help to reduce the cost, improve stability, and enhance activity and selectivity. The

Pt-based bimetallic system is a classic example as Pt is widely used in catalysis. The natural abundance of Pt is extremely low: the concentration of Pt is only 0.005 ppm in earth's crust (~30 times less than Au), and the resulting production of useable Pt is only 133 tons per year (~13 times less than Au) [133]. Minimizing the use of Pt by introducing other cheaper metals is economically favorable for commercializing Pt-based catalysts. Pt was found to be a good catalyst for the hydrogen oxidation reaction (HOR, in anode of fuel cell, H_2 to H^+) and ORR in the proton exchange membrane (PEM) fuel cells [144]. However, the H_2 is usually generated by reforming hydrocarbons and is therefore mixed with a large amount of CO. The CO impurity can severely poison Pt catalysts in the anodes of the fuel cells [145–147]. To produce H_2 without CO, the PROX of CO becomes a key reaction for the better performance of fuel cells. Experimental and theoretical studies have demonstrated that the use of a bimetallic catalyst with a Pt shell on a Ru core has better performance in PROX relative to Pt alone and some other bimetallic systems [140]. Moreover, owing to the acidic environment and high potential of startup/shutdown cycles, the Ru particles can dissolve or agglomerate. The dissolution and agglomeration results in degradation of the Pt–Ru alloy catalyst [148]. The protection provided by the Pt shell increases the stability of the Pt–Ru bimetallic system. Usually the second metal introduced has a slightly different lattice parameter than the parent metal. The lattice strain may have a major impact on the electronic structure of the parent metal. In the Pt–Pd bimetallic system, Pt has a slightly larger lattice constant (3.92 Å for Pt compared to 3.89 Å for Pd). The compressive strain on the Pt surface due to Pd can result in a downshift of the d-band center, which weakens the binding strength of adsorbents [149–151]. The catalytic activities can increase or decrease depending on whether the adsorption or desorption of the intermediates determine the reaction rate [152,153]. For the ORR in acid fuel cells, multifold enhancement of the specific activity was reported for Pt-coated Pd cores and Pt-coated Pd_3Co cores compared to Pt nanoparticles alone [139]. The enhancement was attributed to the lattice mismatch-induced contraction on the Pt surface, which is in agreement with experimental measurements and DFT calculations.

Experimental and theoretical studies have shown that the catalytic performances of bimetallic systems significantly depend on the geometry of the nanoalloys [154,155]. For example, DFT studies suggest that optimum ORR activity occurs with a bilayer of Pt over the Ru core ($\text{Pt}_{2\text{ML}}\text{Ru}$) [156]. Hsieh et al. have shown that ordered $\text{Pt}_{2\text{ML}}\text{Ru}$ nanoparticles can be synthesized and may have applications in PEM fuel cell catalysts [141]. In their synthesis, the Ru nanoparticles were synthesized and successively overcoated with Pt. No organic ligands were used and the synthesis and coating were managed by controlling the reaction temperature and pH values in the solutions. However, based on their X-ray diffraction (XRD) studies, an alloyed interface with intermixing of Pt and Ru was found on the as-prepared core/shell nanoparticles. The authors attributed the intermixing to the surface defects on the Ru nanoparticles. To address this problem,

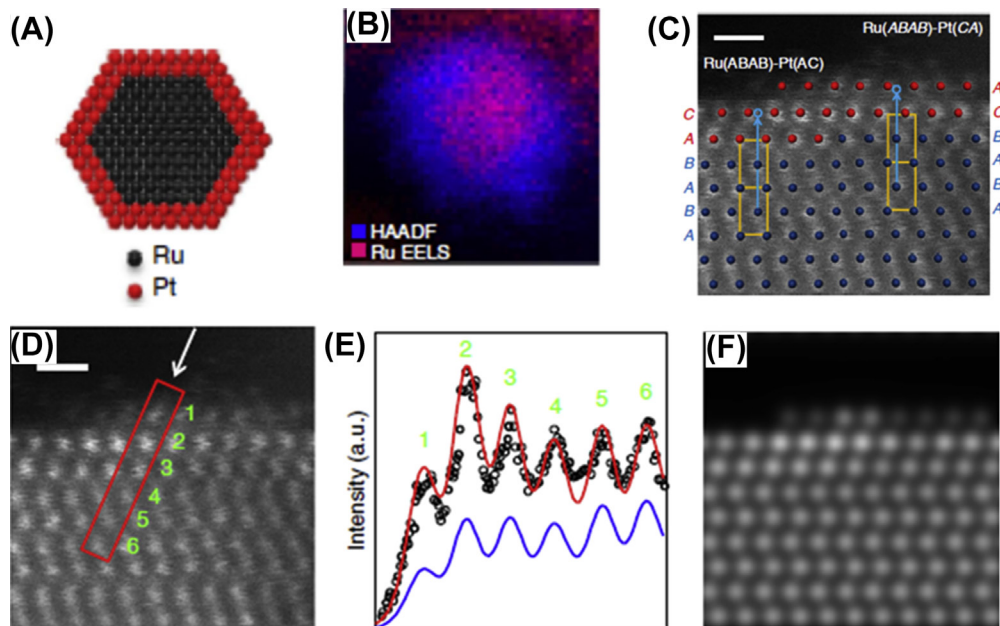


Figure 20 A Pt–Ru core–shell bimetallic catalyst for proton exchange membrane fuel cells. (A) Schematic view of a bilayer Pt overcoating on a Ru core. (B) High angle annular dark field (HAADF) and electron energy loss spectroscopy studies of a Pt–Ru core–shell bimetallic system. (C) An atomic resolution HAADF profile-view image of a bilayer Pt overcoating on Ru core. Scale bar 0.5 nm. (D), (E) Measurement of the intensity profile of surface spots in the HAADF images, as indicated by the red (black in print versions) box in (D). In (E), the black circles denote the intensities on experimental images, the red (black in print versions) line represents the intensities of simulated HAADF images of the Pt–Ru bimetallic system. The blue (gray in print versions) line denotes the intensity profile of a simulated image with only Ru. Scale bar 0.5 nm (F) The simulated ADF images using Pt–Ru core–shell system. Reprinted by permission from Macmillan Publishers Ltd: Hsieh et al. *Nat. Commun.* 4 (2013) <http://dx.doi.org/10.1038/ncomms3466>, copyright 2013.

the Ru nanoparticles were annealed at 450 °C in order to remove the surface lattice defects. The resulting Pt/Ru interface became much shaper based on their XRD, HAADF, and EDS studies. Figure 20(A) shows a schematic model of the Pt_{2ML}Ru system. HAADF and EELS mapping (Figure 20(B)) show a rather uniform Pt shell with a thickness of approximately 2–3 MLs. In addition to the surface chemical composition, the atomic interfacial structure between Pt (111) and Ru (0001) was visualized. Ru has a hcp structure with AB stacking in the [0001] direction while Pt has a fcc structure with an ABC stacking in the [111] direction. By setting the terminating surface of Ru as the B layer, atomic resolution HAADF shows the Pt overlayer can either occupy the A site or C site, as shown in Figure 20(C). The energy difference between the two configurations is small according to their DFT calculations. The stacking shift should be caused by the Pt coating rather than the Ru, as the shifting of the Ru layer is energetically

unfavorable based on their DFT studies as well as previous calculations on the segregations of single crystal surfaces [157]. As has been mentioned, the intensity of the atom spots in ADF images is thickness-dependent. The authors performed image simulation to take into account the decreasing thickness at the edge. The decrease in thickness results in a decrease in intensity. Therefore the increased intensity of the surface atom spots could be confidently assigned to the Pt atoms, as shown in Figure 20(E) and (F).

The Pt_{2ML}Ru catalyst was added into PEM fuel cells. The Pt_{2ML}Ru was demonstrated to be superior to Pt_{1ML}Ru and Pt nanoparticles with regard to HOR activity. After 2500 startup/shutdown cycles, the catalytic performance showed little change. This was attributed to the stable ordered Pt_{2ML}Ru structure. It might be interesting to further develop the bimetallic catalysts, as studies show the introduction of Pd can further prevent the dissolution of Pt to an extent.

For some simple reactions, imaging the surface of a bimetallic catalyst under reaction conditions in ETEMs provides fruitful information toward understanding the atomic origin of the enhanced catalytic activity. Au–Ag is one of the most studied bimetallic systems. The Au–Ag system was found to be more active for CO oxidation than using Au alone [128]. Moreover, the activity can be tuned by varying the ratio of Au and Ag [158–162]. Fujita et al. performed ETEM observations on nanoporous Au (NPG) with 20 at% Ag and NPG with 1.2 at% Ag [163]. Under 1 vol% CO in an air gas mixture at 30 pa, the (110) surface of NPG undergoes significant {111} faceting, as shown in Figure 21(A) and (B). However, NPG with 20 at% Ag maintains a flat surface under the same atmosphere, as shown in Figure 21(C) and (D). The authors attributed the stabilization of the Au surface to the surface Ag atoms, although the contrast difference of Au and Ag is too small to be identified in their experimental HREM images (although it may be detectable if a range of defoci was used). The activity enhancement of NPG in CO oxidation originates in part from the stabilized low-coordinate surface Au atoms at the kinks and step edges. With the help of single-crystal surface studies, the role of surface Ag is better understood. The sputtered Au (111) surface is still not as active as supported Au nanoparticles unless the O is pre-adsorbed [164–167], although the sputtered surface has a large amount of low-coordinate surface Au atoms. DFT studies show that the adsorption of CO may not be influenced significantly by the Ag impurities. However the dissociative adsorption of O₂ can be enhanced by surface Ag impurities [168]. It is worth noting that the surface structure models usually employed for DFT calculations are Au surfaces with Ag atom patches, which is a rather reasonable assumption, as surface segregation of Au–Ag bimetallic nanoparticles is verified by atomic simulations using semiempirical potentials [169]. As one caveat, there are some ambiguities in understanding alloy segregation in nanoparticles including possible substantial deviations from a simple Wulff shape [170]. This is currently a very active area of research with new data from aberration-corrected instruments as well as from other techniques and modeling methods changing how we understand these systems.

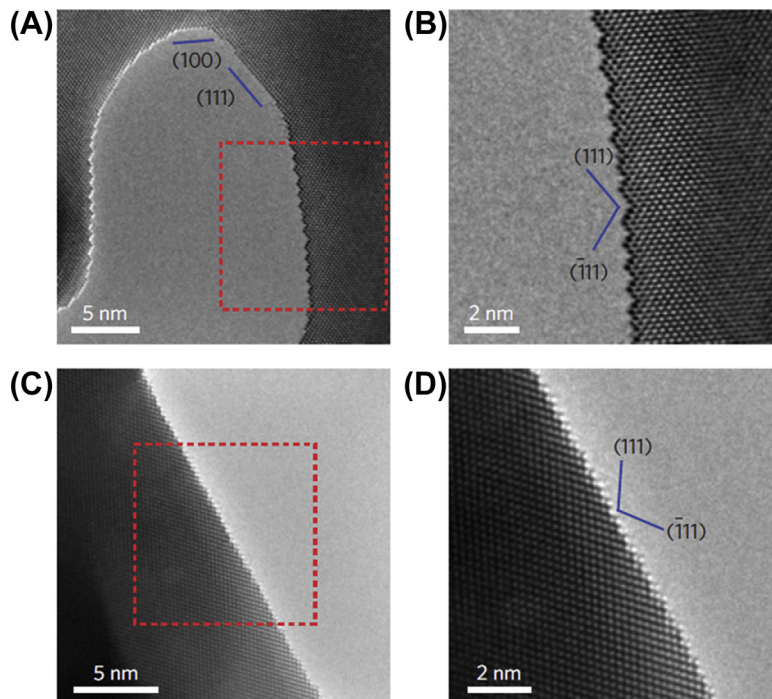


Figure 21 The surface structures of nanoporous gold (NPG) under CO oxidation. (A), (B) High resolution electron microscopy (HREM) images show the presence of (111) faceting on Low-Ag NPG containing 1.2 at% Ag. (C), (D) HREM images show the (111) faceting is not as obvious on the NPG with 20 at% Ag. Reprinted by permission from Macmillan Publishers Ltd: Fujita et al. *Nat. Mater.* 11 (2012) 775–780, copyright 2012.

4.5 Single Atom Catalysts

In heterogeneous catalysis, the active sites of the supported metal are often located on the low-coordinate positions such as the surface, corners, and edge, although there are some catalytic systems where this is not the case; for instance the activity of the catalyst may increase, but the selectivity may be worse. With decreasing size, the density of low-coordinate sites increases. Sometimes an efficient use of a catalytic metal is achieved when the size is reduced to single atoms. Stable single atom catalysts (SACs) have been obtained on oxide supports [7,171,172], metal supports [173,174], graphene sheets [175], zeolites, and metal organic frameworks [176–178]. Superior activities are observed for SACs compared to their multi-atom counterparts when normalized to the number of active sites. Interaction of the metal atom with the support should be considered to obtain a better understanding of SACs. Owing to the extremely small size of the SACs, the electronic effect induced by the support is more significant. For an oxide support, strong bonding between the metal catalyst and the O atoms of the support can result in a positive charge on the SACs [7,179–186]. The positive charge can facilitate gas

adsorption and affect catalytic performance. It was demonstrated that the positively charged Au and Pt species on CeO₂ supports are responsible for high activity in the WGS [181]. For metal and graphene supports, the lattice strain can result in a change of d-band states [173,175], which can also influence catalytic performance. A common concern about the SACs is the stability issue, as low-coordinate SACs should result in high surface free energy. However some SACs appear to be rather stable: high activity is generally maintained after multiple reaction cycles at elevated temperature. The stability is usually attributed to strong anchoring of the single atom site by the support. The anchoring mechanisms have been investigated for Au–CeO₂ [41,43,61,181,187,188], Pt–CeO₂ [181,189], Pt–Al₂O₃ [190,191], Pd–Al₂O₃ [179], Ag–MnO₂ [192], and other supported metal systems [193]. The strong anchoring may not only help to stabilize the SACs, but also the support. For example, it was found that La single atoms on the surface of γ -Al₂O₃ can help to prevent the phase transformation of the γ -Al₂O₃ to the more stable α -Al₂O₃ [194]. The exact anchoring sites vary from system to system. Experimental verification and theoretical calculations should be conducted for each specific system to develop a complete understanding.

Aberration-corrected HAADF imaging at sub-Å resolution is capable of resolving single atoms, which provides a convenient method to check whether or not the catalysts are atomically well dispersed. Moreover, plan-view imaging is capable of visualizing the anchoring sites of catalyst atoms on a support. A good example is demonstrated by Chang et al. in studying the adsorption site of Pt on the (110) surface of a rutile TiO₂ (110) single crystal [195]. TiO₂ is widely used in chemical catalysis [117,123] and photocatalysis [196–198]. The (110) surface of TiO₂ is treated as a model surface and has been extensively studied [199]. The structural model is shown in Figure 22(A). The (1 × 1) TiO₂ (110) surface consists of two types of Ti and O atoms. The extrusion two-fold coordinated O (O_{2c}) are bridging atoms on Ti atoms (Ti_{6c}) at the base layer. The rows of Ti_{6c} atoms running in the [001] direction separate the fivefold coordinated Ti atoms (Ti_{5c}), which are bonded with threefold coordinated O atoms (O_{3c}). The O_{2c} atoms can act as Brønsted bases which can adsorb H while the Ti_{5c} atoms act as Lewis acid sites for adsorbing organic molecules [200]. O_{3c} and Ti_{6c} are usually considered as bulk species because they have the same coordination number as in the bulk. On vacuum-prepared TiO₂ (110) surfaces, a small percentage of O_{2c} atoms are missing, which is often observed in STM studies [199,201]. The resulting vacancies (O_{br} vacancies) are often considered to be stable adsorption sites for Pt atoms in DFT studies [202,203]. Surprisingly, Chang et al. observed that Pt atoms are preferentially adsorbed onto the position of missing O_{3c} atoms (O_{ba} vacancies). If eight possible adsorption sites are considered on both stoichiometric and reduced surfaces, five of them can be clearly identified by their HAADF images, as shown in Figure 22(C). The unidentifiable adsorption sites are as such because plan-view HAADF images are not very sensitive to the difference in thickness between one or several layers (it is possible that the surface is not

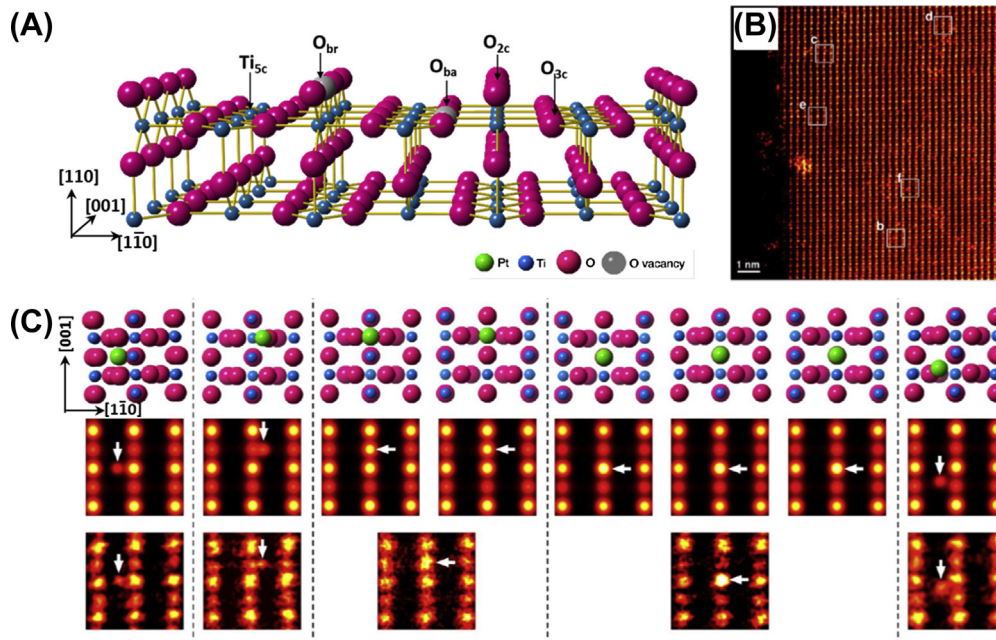


Figure 22 Adsorption sites of Pt atoms on a rutile TiO_2 (110) surface. (A) A structural model of atoms and defects on a TiO_2 (110) surfaces. (B) An experimental atomic resolution high angle annular dark field (HAADF) image of Pt on a TiO_2 (110) surfaces. (C) Structural models, experimental and simulated HAADF images of Pt adsorption sites on TiO_2 (110), as indicated in (B). Panels (B) and (C) were adapted with permission from Chang et al. *Nano Lett.* 14 (2014) 134–138. Copyright (2014) American Chemical Society.

atomically flat). However, the frequency of adsorption at O_{br} vacancies is statistically the highest. Their DFT calculation (GGA + U) shows that creating O_{br} vacancies requires less energy than the formation of O_{ba} vacancies (0.15 eV), which implies that the predominant O vacancies on the vacuum annealed surface are O_{br} vacancies. However, the highest binding energy of Pt on the surface was on the adsorption on O_{ba} vacancies in all of the eight sites considered, which is 0.18 eV higher than the adsorption on the O_{br} vacancies. Thus, it is possible that the O_{ba} vacancies are created due to the presence of Pt atoms and provide the anchoring sites for Pt atoms.

Tao Zhang's group has investigated SACs on FeO_x supports [7]. The Pt– FeO_x SACs exhibit significantly higher activity for CO oxidation compared to Pt– FeO_x with 3D Pt clusters as well as the standard Au– Fe_2O_3 catalyst. The Pt atoms were found to occupy the Fe sites on the (100) surface based on plan-view HAADF images. One type of FeO_x , $\alpha\text{-Fe}_2\text{O}_3$, has a hexagonal corundum structure. Under the [0001] direction, it has a repeated stacking of Fe–Fe– O_3 –... layers. Hence the termination surface can be a single layer of Fe, a double layer of Fe, or an O_3 layer. Experimental and theoretical studies indicated that the surface can have mixed terminations [204–209]. It is possible that

under O-rich conditions, O₃ terminated surface is preferred. The Fe terminated surface is favorable under O-deficient conditions [204]. Based on the HAADF results (see Figure 4(B)), the DFT calculations show that the most stable position for Pt is on the O₃-terminated (0001) surface. The Pt atoms occupy the threefold hollow sites on the O₃ layer, which can be understood as a replacement of the Fe atoms for the single Fe termination. The Pt atoms on the O₃ layer can also reduce the surface O vacancy formation energy and enhance the catalytic activity for CO oxidation. The Bader charge analysis suggests that the Pt is positively charged (+0.45|e|), which was confirmed experimentally by FT-IR.

The same group demonstrated that Ir-FeO_x SACs show even higher catalytic activity for the WGS reaction than Pt-FeO_x SACs [171]. The activity is one order of magnitude higher than that was observed for Ir nanoparticles or clusters on FeO_x supports. By increasing the loading of Ir, the size of the Ir catalysts can be tuned from single atoms to a mixture of single atoms and clusters, and decreasing the loading results in a higher percentage of single atoms sites. By comparing the TOFs of the catalysts with difference loadings, an interesting finding is that the single atom sites contribute to ~70% of the activity. This suggests that the single atom sites are the most important active sites for WGS. The high activities can be maintained over 20h of reaction time. Additionally, HAADF-STEM images confirmed that after that reaction, the catalysts were primarily SACs. The long-term stability and enhanced activity were explained the similar way as for the Pt SACs on FeO_x. The Ir SACs were found to occupy the Fe positions and they were positively charged according to X-ray absorption near-edge structure (XANES). In addition, the H₂ TPR shows that the formation of O vacancies is facilitated by the Ir SACs.

HAADF imaging has also been used to study SACs on porous zeolites [210,211]. As zeolites are more sensitive to the electron beam compared to oxide supports, low dose imaging was usually employed for characterizing such materials. The signal-to-noise ratios in these images are relatively low due to the low electron dose. However, useful structural information can still be extracted based on image processing. For example, Ortalan et al. investigated the anchoring positions of Ir atoms on a dealuminated HY (DAY) zeolite [210]. They found that more Ir atoms were anchored to the T6 sites compared to the T5 sites of the zeolite crystal. After treating the Ir-zeolite sample in H₂ flow at 393K for 30 min, Ir clusters start to form preferentially on the T6 sites. Therefore, the authors deduced that some Ir atoms anchored to the T5 sites migrate to the T6 sites during the treatment.

5. SUMMARY AND OUTLOOK

In this review, we discussed how the structures and chemical compositions of catalytic systems can be characterized using TEM. The development of TEM has enabled the characterization of catalytic nanoparticles with atomic resolution under reaction conditions, which has significantly helped with understanding catalyst structures and reaction

mechanisms. Currently, direct characterization of catalytic reactions using TEM is limited to the catalyst itself. Adsorption can be observed by TEM by imaging the surface relaxation or other morphological changes on the catalyst. However, direct imaging of the adsorption of reactant molecules on the catalytic active sites is still a great difficulty. This is partly because the contrast of the small amount of light molecules is too low compared to that of the catalyst itself, both in the imaging and spectroscopic techniques of TEM. Recently Yoshida et al. suggested that the adsorbed CO molecules could be directly imaged by using aberration-corrected ETEM [119]. However, the signal from the CO is rather low and should be confirmed by other techniques. Increasing the electron dose during characterization may increase the contrast. However, high electron dose can cause desorption of molecules [212,213] and even damage the catalyst [55,214]. New techniques such as exit wave reconstruction, which numerically “adds” a set of low dose images to increase the contrast [215–218], may allow for imaging of the adsorbates. While it is relatively difficult using TEM, other techniques such as FT-IR and Raman are good at characterizing the adsorption and desorption phenomena. A comprehensive understanding of the properties of catalysts requires the employment of different characterization techniques and theoretical studies.

The main focus of this chapter has been methods of looking at catalysts using electron microscopy, mainly at the atomic scale. It is appropriate at the end to step back slightly with a few words of caution, the three R’s: Radiation damage, Rigor, and Reality.

Radiation Damage: The environment of any electron microscope is harsh, not just the vacuum but also because of energetic energy loss processes. It is sometimes easy to damage materials, and on rare occasions to heat them using the electron beam. The simplest process is direct momentum transfer, called knock-on damage, which occurs whenever the electron energy is above some threshold which depends upon not just the atomic mass but also the bonding. In many cases this can be minimized by using lower voltages. However, there is a second damage process, radiolysis, which becomes more common if the voltage is reduced and is very significant for oxides as well as chemisorbed species. Some years ago the group of Yagi et al. built a UHV electron microscope which was capable of doing both lower resolution reflection electron microscopy (REM) of surfaces and photoelectron electron microscopy (PEEM), the aim being to image chemisorbed species on silicon using PEEM and correlate this with surface structure using REM. Unfortunately it turned out that the chemisorbed species were completely removed by the microscope beam [219]. The electron flux that they used was several orders of magnitude smaller than what one has in contemporary instruments. While it is possible that there will be an equilibrium chemisorbed surface concentration in ETEM experiments, the extent to which they are imaged is unclear.

Rigor: The first images of single atoms in a home built STEM instrument was reported by the group of Crewe in the 1970s (e.g., Refs [220–226]) and when commercial instruments became available these instruments became a staple method of

examining catalysts (e.g., Refs [227,228]). Atomic imaging of small particles became relatively easy in the early 1980s, although there were papers such as the elegant work of Tsutomu [229] and surface studies at lower resolution [230–237] much earlier. Profile imaging was discovered in the early 1980s [11,238–240], and was rapidly used and extended by many groups around the world for both profile and plan-view imaging using instruments without aberration correctors (e.g., Refs [235,241–256]), see also [257] for other early references. Because those instruments had lanthanum hexaboride sources it was relatively easy to image the surface (as well as the bulk) [258]. When brighter and more coherent field emission sources became common, it in fact became much harder to image surfaces; it was only when aberration-correctors became common that surfaces could be imaged as easily as they were in the 1980s. For certain the newer corrected instruments are better, but at the same time they are sometimes used on problems which were extensively studied some years earlier, for instance the reconstruction on the gold (001) surface [259].

Reality: It is sometimes possible to generate a model to explain what images of nanoparticles used in catalysts mean in terms of the local structure. Unfortunately that does not prove that the model is unique. While coupling electron microscopy with DFT calculations is very powerful, at the same time this still does not make the interpretation unique. Methods such as DFT only lead to a local minimum, so if the initial atomic structure model used is not appropriate then the results they yield will only be better than the initial guess, not necessarily right. Sometimes DFT can be problematic by itself, for instance the well-known errors in chemisorption energies with simple functionals. One always has to worry whether an interpretation conforms to how the sample was made, basic thermodynamics as well as Occam's razor.

Are we at the limits of what can be achieved in imaging catalysts? The answer is no, and in the next few years there may well be much more information. We have already crossed the barrier of being able to image nanoparticles in three-dimensions at the atomic scale [260] with a three dimensional resolution of $2 \times 2 \times 2 \text{ \AA}^3$ voxels. We expect that within a few years we will see measurements of, for instance, the positions of all atoms in bimetallic nanoparticles with three dimensional precision of 0.5 \AA , as well as three dimensional chemical mapping and perhaps even mapping in three dimensions of chemical shifts.

ACKNOWLEDGMENTS

Part of this work is supported by the funding from the Northwestern University Institute for Catalysis in Energy Processes (ICEP) on grant number DOE DE-FG02-03-ER15457. K.R.P. would like to thank the funding from the Institute for Atom-Efficient Chemical Transformations (IACT), an Energy Frontier Research Center funded by the U.S. Department of Energy, Office of Science, Office of Basic Energy Sciences. The authors also thank the contribution from Jianguo Wen, James A. Enterkin, Zili Wu, Linhua Hu, and Robert M. Kennedy. Part of HREM images are obtained using the facilities at the Electron Microscopy Center for Materials Research at Argonne National Laboratory.

REFERENCES

- [1] Y. Zhu, H. Inada, K. Nakamura, J. Wall, *Nat. Mater.* 8 (2009) 808–812.
- [2] S. Takeda, H. Yoshida, *Microscopy* 62 (2013) 193–203.
- [3] M. De Graef, *Introduction to Conventional Transmission Electron Microscopy*, Cambridge University Press, Cambridge, 2003.
- [4] D.B. Williams, C.B. Carter, *Transmission Electron Microscopy: A Textbook for Materials Science*, Springer, New York, 2009.
- [5] S.J. Pennycook, P.D. Nellist, *Scanning Transmission Electron Microscopy: Imaging and Analysis*, Springer, New York, 2011.
- [6] J.M. Cowley, *Appl. Phys. Lett.* 15 (1969) 58–59.
- [7] B. Qiao, A. Wang, X. Yang, L.F. Allard, Z. Jiang, Y. Cui, J. Liu, J. Li, T. Zhang, *Nat. Chem.* 3 (2011) 634–641.
- [8] G. Jayaram, R. Plass, L.D. Marks, *Interface Sci.* 2 (1995) 379–395.
- [9] E. Bengu, R. Plass, L.D. Marks, T. Ichihashi, P.M. Ajayan, S. Iijima, *Phys. Rev. Lett.* 77 (1996) 4226.
- [10] Y. Kuwauchi, S. Takeda, H. Yoshida, K. Sun, M. Haruta, H. Kohno, *Nano Lett.* 13 (2013) 3073–3077.
- [11] L.D. Marks, D.J. Smith, *Nature* 303 (1983) 316–317.
- [12] R. Yu, L.H. Hu, Z.Y. Cheng, Y.D. Li, H.Q. Ye, J. Zhu, *Phys. Rev. Lett.* 105 (2010) 226101.
- [13] Y. Lin, Z. Wu, J. Wen, K.R. Poeppelmeier, L.D. Marks, *Nano Lett.* 14 (2014) 191–196.
- [14] Y. Lin, J. Wen, L. Hu, R.M. Kennedy, P.C. Stair, K.R. Poeppelmeier, L.D. Marks, *Phys. Rev. Lett.* 111 (2013) 156101.
- [15] L.P. Hansen, Q.M. Ramasse, C. Kisielowski, M. Brorson, E. Johnson, H. Topsøe, S. Helveg, *Angew. Chem. Int. Ed.* 50 (2011) 10153–10156.
- [16] N. Alem, Q.M. Ramasse, C.R. Seabourne, O.V. Yazyev, K. Erickson, M.C. Sarahan, C. Kisielowski, A.J. Scott, S.G. Louie, A. Zettl, *Phys. Rev. Lett.* 109 (2012) 205502.
- [17] N. Lu, Q. Wan, J. Zhu, *J. Phys. Chem. Lett.* 1 (2010) 1468–1471.
- [18] M.-R. He, R. Yu, J. Zhu, *Nano Lett.* 12 (2012) 704–708.
- [19] O. Scherzer, *J. Appl. Phys.* 20 (1949) 20–29.
- [20] M. Haider, H. Rose, S. Uhlemann, B. Kabius, K. Urban, *J. Electron Microsc.* 47 (1998) 395–405.
- [21] O.L. Krivanek, N. Dellby, A.R. Lupini, *Ultramicroscopy* 78 (1999) 1–11.
- [22] C. Kisielowski, B. Freitag, M. Bischoff, et al., *Microsc. Microanal.* 14 (2008) 469–477.
- [23] D. Van Dyck, M. Op de Beeck, *Ultramicroscopy* 64 (1996) 99–107.
- [24] C.-L. Jia, Markus Lentzen, K. Urban, *Microsc. Microanal.* 10 (2004) 174–184.
- [25] R. Kilaas, MacTempas, <http://www.totalresolution.com/>.
- [26] P.A. Stadelmann, JEMS, <http://cimewww.epfl.ch/people/stadelmann/jemsWebSite/jems.html>.
- [27] K. Ishizuka, xHREM, <http://www.hremresearch.com/Eng/simulation.html>.
- [28] J.M. Zuo, J.C. Mabon, *Microsc. Microanal.* 10 (Suppl. 2) (2004).
- [29] C.T. Koch, QSTEM, http://elim.physik.uni-ulm.de/?page_id=834.
- [30] M.A. Okeefe, R. Kilaas, *Scanning Microsc.* (1988) 225–244.
- [31] S.D. Findlay, N. Shibata, H. Sawada, E. Okunishi, Y. Kondo, Y. Ikuhara, *Ultramicroscopy* 110 (2010) 903–923.
- [32] E. Okunishi, H. Sawada, Y. Kondo, *Micron* 43 (2012) 538–544.
- [33] A. Trovarelli, *Catal. Rev.* 38 (1996) 439–520.
- [34] C. Ratnasamy, J.P. Wagner, *Catal. Rev.* 51 (2009) 325–440.
- [35] J. Beckers, G. Rothenberg, *Green Chem.* 12 (2010) 939–948.
- [36] L. Vivier, D. Duprez, *ChemSusChem* 3 (2010) 654–678.
- [37] M. Mogensen, N.M. Sammes, G.A. Tompsett, *Solid State Ionics* 129 (2000) 63–94.
- [38] S. Park, J.M. Vohs, R.J. Gorte, *Nature* 404 (2000) 265–267.
- [39] A. Atkinson, S. Barnett, R.J. Gorte, J.T.S. Irvine, A.J. McEvoy, M. Mogensen, S.C. Singhal, J. Vohs, *Nat. Mater.* 3 (2004) 17–27.
- [40] J. Kašpar, P. Fornasiero, M. Graziani, *Catal. Today* 50 (1999) 285–298.
- [41] J.A. Farmer, C.T. Campbell, *Science* 329 (2010) 933–936.
- [42] C.T. Campbell, C.H.F. Peden, *Science* 309 (2005) 713–714.
- [43] N. Ta, J. Liu, S. Chenna, P.A. Crozier, Y. Li, A. Chen, W. Shen, *J. Am. Chem. Soc.* 134 (2012) 20585–20588.

- [44] H.-F. Wang, X.-Q. Gong, Y.-L. Guo, Y. Guo, G.Z. Lu, P. Hu, *J. Phys. Chem. C* 113 (2009) 10229–10232.
- [45] H.-F. Wang, H.-Y. Li, X.-Q. Gong, Y.-L. Guo, G.-Z. Lu, P. Hu, *PCCP* 14 (2012) 16521–16535.
- [46] Y. Tang, H. Zhang, L. Cui, C. Ouyang, S. Shi, W. Tang, H. Li, J.-S. Lee, L. Chen, *Phys. Rev. B* 82 (2010) 125104.
- [47] S. Agarwal, L. Lefferts, B.L. Mojet, et al., *ChemSusChem* 6 (2013) 1898–1906.
- [48] P.W. Tasker, *J. Phys. C: Solid State* 12 (1979) 4977.
- [49] J.A. Enterkin, A.E. Becerra-Toledo, K.R. Poepelmeier, L.D. Marks, *Surf. Sci.* 606 (2012) 344–355.
- [50] C. Noguera, *J. Phys. Condens. Matter* 12 (2000) R367.
- [51] J. Goniakowski, F. Finocchi, C. Noguera, *Rep. Prog. Phys.* 71 (2008) 016501.
- [52] P.A. Crozier, R. Wang, R. Sharma, *Ultramicroscopy* 108 (2008) 1432–1440.
- [53] N.V. Skorodumova, S.I. Simak, B.I. Lundqvist, I.A. Abrikosov, B. Johansson, *Phys. Rev. Lett.* 89 (2002) 166601.
- [54] S. Turner, S. Lazar, B. Freitag, R. Egoavil, J. Verbeeck, S. Put, Y. Strauven, G. Van Tendeloo, *Nanoscale* 3 (2011) 3385–3390.
- [55] S.J. Haigh, N.P. Young, H. Sawada, K. Takayanagi, A.I. Kirkland, *ChemPhysChem* 12 (2011) 2397–2399.
- [56] Z. Wu, M. Li, D.R. Mullins, S.H. Overbury, *ACS Catal.* 2 (2012) 2224–2234.
- [57] D.J.M. Bevan, *J. Inorg. Nucl. Chem.* 1 (1955) 49–59.
- [58] C. Binet, M. Daturi, J.-C. Lavalley, *Catal. Today* 50 (1999) 207–225.
- [59] H. Nörenberg, J.H. Harding, *Surf. Sci.* 477 (2001) 17–24.
- [60] O. Dulub, U. Diebold, G. Kresse, *Phys. Rev. Lett.* 90 (2003) 016102.
- [61] F. Esch, S. Fabris, L. Zhou, T. Montini, C. Africh, P. Fornasiero, G. Comelli, R. Rosei, *Science* 309 (2005) 752–755.
- [62] S. Torbrügge, M. Reichling, A. Ishiyama, S. Morita, Ó. Custance, *Phys. Rev. Lett.* 99 (2007) 056101.
- [63] D.C. Grinter, R. Ithnin, C.L. Pang, G. Thornton, *J. Phys. Chem. C* 114 (2010) 17036–17041.
- [64] G.E. Murgida, M.V. Ganduglia-Pirovano, *Phys. Rev. Lett.* 110 (2013) 246101.
- [65] A. Ohtomo, D.A. Muller, J.L. Grazul, H.Y. Hwang, *Nature* 419 (2002) 378–380.
- [66] S. Thiel, G. Hammerl, A. Schmehl, C.W. Schneider, J. Mannhart, *Science* 313 (2006) 1942–1945.
- [67] N. Reyren, S. Thiel, A.D. Caviglia, et al., *Science* 317 (2007) 1196–1199.
- [68] J.G. Mavroides, J.A. Kafalas, D.F. Kolesar, *Appl. Phys. Lett.* 28 (1976) 241–243.
- [69] B. Ura, J. Trawczyński, A. Kotarba, W. Bieniasz, M.J. Illán-Gómez, A. Bueno-López, F.E. López-Suárez, *Appl. Catal. B: Environ.* 101 (2011) 169–175.
- [70] F.A. Rabuffetti, H.-S. Kim, J.A. Enterkin, Y. Wang, C.H. Lanier, L.D. Marks, K.R. Poepelmeier, *P.C. Stair, Chem. Mater.* 20 (2008) 5628–5635.
- [71] F. Dang, K.-i. Mimura, K. Kato, H. Imai, S. Wada, H. Haneda, M. Kuwabara, *CrystEngComm* 13 (2011) 3878–3883.
- [72] L. Hu, C. Wang, S. Lee, R.E. Winans, L.D. Marks, K.R. Poepelmeier, *Chem. Mater.* 25 (2013) 378–384.
- [73] E. Ringe, R.P. Van Duyne, L.D. Marks, *J. Phys. Chem. C* 117 (2013) 15859–15870.
- [74] J.A. Enterkin, W. Setthapun, J.W. Elam, S.T. Christensen, F.A. Rabuffetti, L.D. Marks, P.C. Stair, K.R. Poepelmeier, C.L. Marshall, *ACS Catal.* 1 (2011) 629–635.
- [75] N. Erdman, K.R. Poepelmeier, M. Asta, O. Warschkow, D.E. Ellis, L.D. Marks, *Nature* 419 (2002) 55–58.
- [76] K. Johnston, M.R. Castell, A.T. Paxton, M.W. Finnis, *Phys. Rev. B* 70 (2004) 085415.
- [77] B. Cord, R. Courths, *Surf. Sci.* 162 (1985) 34–38.
- [78] F. Silly, D.T. Newell, M.R. Castell, *Surf. Sci.* 600 (2006) 219–223.
- [79] Q.D. Jiang, J. Zegenhagen, *Surf. Sci.* 338 (1995) L882–L888.
- [80] C.H. Lanier, A. van de Walle, N. Erdman, E. Landree, O. Warschkow, A. Kazimirov, K.R. Poepelmeier, J. Zegenhagen, M. Asta, L.D. Marks, *Phys. Rev. B* 76 (2007) 045421.
- [81] N. Erdman, O. Warschkow, M. Asta, K.R. Poepelmeier, D.E. Ellis, L.D. Marks, *J. Am. Chem. Soc.* 125 (2003) 10050–10056.
- [82] G.-z. Zhu, G. Radtke, G.A. Botton, *Nature* 490 (2012) 384–387.
- [83] M.R. Castell, *Surf. Sci.* 516 (2002) 33–42.

- [84] R. Hergert, P.R. Willmott, O. Bunk, C.M. Schlepütz, B.D. Patterson, B. Delley, *Phys. Rev. Lett.* 98 (2007) 076102.
- [85] D.M. Kienzle, A.E. Becerra-Toledo, L.D. Marks, *Phys. Rev. Lett.* 106 (2011) 176102.
- [86] M. Kawasaki, K. Takahashi, T. Maeda, R. Tsuchiya, M. Shinohara, O. Ishiyama, T. Yonezawa, M. Yoshimoto, H. Koinuma, *Science* 266 (1994) 1540–1542.
- [87] S.B. Lee, F. Phillipp, W. Sigle, M. Rühle, *Ultramicroscopy* 104 (2005) 30–38.
- [88] J.D. Baniecki, M. Ishii, K. Kurihara, K. Yamanaka, T. Yano, K. Shinozaki, T. Imada, K. Nozaki, N. Kin, *Phys. Rev. B* 78 (2008) 195415.
- [89] R. Sum, R. Lüthi, H.P. Lang, H.J. Güntherodt, *Phys. C: Supercond.* 235–240 (Part 1) (1994) 621–622.
- [90] S.S. Sheiko, M. Möller, E.M.C.M. Reuvekamp, H.W. Zandbergen, *Phys. Rev. B* 48 (1993) 5675–5678.
- [91] K. Szot, W. Speier, *Phys. Rev. B* 60 (1999) 5909–5926.
- [92] K. Szot, W. Speier, U. Breuer, R. Meyer, J. Szade, R. Waser, *Surf. Sci.* 460 (2000) 112–128.
- [93] K. Szot, W. Speier, J. Herion, C. Freiburg, *Appl. Phys. A* 64 (1996) 55–59.
- [94] A. Gunhold, K. Gömann, L. Beuermann, M. Frerichs, G. Borchardt, V. Kempter, W. Maus-Friedrichs, *Surf. Sci.* 507–510 (2002) 447–452.
- [95] J.A. Lopez-Sanchez, N. Dimitratos, C. Hammond, et al., *Nat. Chem.* 3 (2011) 551–556.
- [96] Y. Yamada, C.-K. Tsung, W. Huang, Z. Huo, S.E. Habas, T. Soejima, C.E. Aliaga, G.A. Somorjai, P. Yang, *Nat. Chem.* 3 (2011) 372–376.
- [97] D. Zanchet, H. Tolentino, M.C. Martins Alves, O.L. Alves, D. Ugarte, *Chem. Phys. Lett.* 323 (2000) 167–172.
- [98] G. Corthey, A.A. Rubert, A.L. Picone, et al., *J. Phys. Chem. C* 116 (2012) 9830–9837.
- [99] T. Bligaard, J.K. Nørskov, *Electrochim. Acta* 52 (2007) 5512–5516.
- [100] F. Behafarid, J. Matos, S. Hong, L. Zhang, T.S. Rahman, B. Roldan Cuenya, *ACS Nano* 8 (2014) 6671–6681.
- [101] A.D. Polli, T. Wagner, T. Gemming, M. Rühle, *Surf. Sci.* 448 (2000) 279–289.
- [102] V. Komanicky, H. Iddir, K.-C. Chang, A. Menzel, G. Karapetrov, D. Hennessy, P. Zapol, H. You, *J. Am. Chem. Soc.* 131 (2009) 5732–5733.
- [103] C.J. Kliewer, M. Bieri, G.A. Somorjai, *J. Am. Chem. Soc.* 131 (2009) 9958–9966.
- [104] C.-L. Jia, S.-B. Mi, K. Urban, I. Vrejoiu, M. Alexe, D. Hesse, *Nat. Mater.* 7 (2008) 57–61.
- [105] X. Xiao, X. Liu, H. Zhao, D. Chen, F. Liu, J. Xiang, Z. Hu, Y. Li, *Adv. Mater.* 24 (2012) 5762–5766.
- [106] Y. Wang, H.J. Zhang, J. Wei, C.C. Wong, J. Lin, A. Borgna, *Energy Environ. Sci.* 4 (2011) 1845–1854.
- [107] L. Hu, Q. Peng, Y. Li, *J. Am. Chem. Soc.* 130 (2008) 16136–16137.
- [108] L. Hu, K. Sun, Q. Peng, B. Xu, Y. Li, *Nano Res.* 3 (2010) 363–368.
- [109] X. Xie, Y. Li, Z.-Q. Liu, M. Haruta, W. Shen, *Nature* 458 (2009) 746–749.
- [110] J. Xiao, Q. Kuang, S. Yang, F. Xiao, S. Wang, L. Guo, *Sci. Rep.* 3 (2013).
- [111] L. Vitos, A.V. Ruban, H.L. Skriver, J. Kollár, *Surf. Sci.* 411 (1998) 186–202.
- [112] R. Kaischew, *Arbeitsstag. Festkörper Phys.* (1952) 81.
- [113] W.L. Winterbottom, *Acta Metall.* 15 (1967) 303–310.
- [114] J.A. Enterkin, K.R. Poeppelmeier, L.D. Marks, *Nano Lett.* 11 (2011) 993–997.
- [115] J. Enterkin, R. Kennedy, J. Lu, J. Elam, R. Cook, L. Marks, P. Stair, C. Marshall, K. Poeppelmeier, *Top. Catal.* 56 (2013) 1829–1834.
- [116] P.L. Hansen, J.B. Wagner, S. Helveg, J.R. Rostrup-Nielsen, B.S. Clausen, H. Topsøe, *Science* 295 (2002) 2053–2055.
- [117] Y. Kuwauchi, H. Yoshida, T. Akita, M. Haruta, S. Takeda, *Angew. Chem. Int. Ed.* 51 (2012) 7729–7733.
- [118] T. Uchiyama, H. Yoshida, Y. Kuwauchi, S. Ichikawa, S. Shimada, M. Haruta, S. Takeda, *Angew. Chem. Int. Ed.* 50 (2011) 10157–10160.
- [119] H. Yoshida, Y. Kuwauchi, J.R. Jinschek, K. Sun, S. Tanaka, M. Kohyama, S. Shimada, M. Haruta, S. Takeda, *Science* 335 (2012) 317–319.
- [120] B. Hammer, J.K. Nørskov, *Nature* 376 (1995) 238–240.
- [121] G.C. Bond, *Catal. Today* 72 (2002) 5–9.
- [122] A. Franceschetti, S.J. Pennycook, S.T. Pantelides, *Chem. Phys. Lett.* 374 (2003) 471–475.
- [123] M. Haruta, S. Tsubota, T. Kobayashi, H. Kageyama, M.J. Genet, B. Delmon, *J. Catal.* 144 (1993) 175–192.

- [124] M.S. Chen, D.W. Goodman, *Science* 306 (2004) 252–255.
- [125] B.Yoon, H. Häkkinen, U. Landman, *J. Phys. Chem.* 107 (2003) 4066–4071.
- [126] J. Guzman, B.C. Gates, *J. Am. Chem. Soc.* 126 (2004) 2672–2673.
- [127] M. Mavrikakis, P. Stoltze, J.K. Nørskov, *Catal. Lett.* 64 (2000) 101–106.
- [128] X.Y. Liu, A. Wang, T. Zhang, C.-Y. Mou, *Nano Today* 8 (2013) 403–416.
- [129] O. Lopez-Acevedo, K.A. Kacprzak, J. Akola, H. Häkkinen, *Nat. Chem.* 2 (2010) 329–334.
- [130] Z. Wu, M. Li, S.H. Overbury, *J. Catal.* 285 (2012) 61–73.
- [131] K.-i. Fukui, Y. Namai, Y. Iwasawa, *Appl. Surf. Sci.* 188 (2002) 252–256.
- [132] D.A. Siegel, W.C. Chueh, F. El Gabaly, K.F. McCarty, J. de la Figuera, M. Blanco-Rey, *J. Chem. Phys.* 139 (2013) 114703.
- [133] H. Zhang, M. Jin, Y. Xia, *Chem. Soc. Rev.* 41 (2012) 8035–8049.
- [134] C. Sun, H. Li, L. Chen, *Energy Environ. Sci.* 5 (2012) 8475–8505.
- [135] J. Lu, B. Fu, M.C. Kung, G. Xiao, J.W. Elam, H.H. Kung, P.C. Stair, *Science* 335 (2012) 1205–1208.
- [136] F. Besenbacher, I. Chorkendorff, B.S. Clausen, B. Hammer, A.M. Molenbroek, J.K. Nørskov, I. Stensgaard, *Science* 279 (1998) 1913–1915.
- [137] G.W. Huber, J.W. Shabaker, J.A. Dumesic, *Science* 300 (2003) 2075–2077.
- [138] L. Liu, G. Samjeske, S.-i. Nagamatsu, O. Sekizawa, K. Nagasawa, S. Takao, Y. Imaizumi, T. Yamamoto, T. Uruga, Y. Iwasawa, *J. Phys. Chem. C* 116 (2012) 23453–23464.
- [139] J.X. Wang, H. Inada, L. Wu, Y. Zhu, Y. Choi, P. Liu, W.-P. Zhou, R.R. Adzic, *J. Am. Chem. Soc.* 131 (2009) 17298–17302.
- [140] S. Alayoglu, A.U. Nilekar, M. Mavrikakis, B. Eichhorn, *Nat. Mater.* 7 (2008) 333–338.
- [141] Y.-C. Hsieh, Y. Zhang, D. Su, et al., *Nat. Commun.* 4 (2013).
- [142] H. Zhang, M. Jin, H. Liu, J. Wang, M.J. Kim, D. Yang, Z. Xie, J. Liu, Y. Xia, *ACS Nano* 5 (2011) 8212–8222.
- [143] A.T. Bell, *Science* 299 (2003) 1688–1691.
- [144] H.A. Gasteiger, S.S. Kocha, B. Sompalli, F.T. Wagner, *Appl. Catal. B: Environ.* 56 (2005) 9–35.
- [145] L. Carrette, K.A. Friedrich, U. Stimming, *ChemPhysChem* 1 (2000) 162–193.
- [146] S.J. Lee, S. Mukerjee, E.A. Ticianelli, J. McBreen, *Electrochim. Acta* 44 (1999) 3283–3293.
- [147] S.J.C. Cleghorn, X. Ren, T.E. Springer, M.S. Wilson, C. Zawodzinski, T.A. Zawodzinski, S. Gottesfeld, *Int. J. Hydrogen Energy* 22 (1997) 1137–1144.
- [148] R. Borup, J. Meyers, B. Pivovar, et al., *Chem. Rev.* 107 (2007) 3904–3951.
- [149] L. Grabow, Y. Xu, M. Mavrikakis, *PCCP* 8 (2006) 3369–3374.
- [150] M. Mavrikakis, B. Hammer, J.K. Nørskov, *Phys. Rev. Lett.* 81 (1998) 2819–2822.
- [151] Y. Xu, A.V. Ruban, M. Mavrikakis, *J. Am. Chem. Soc.* 126 (2004) 4717–4725.
- [152] J.X. Wang, J. Zhang, R.R. Adzic, *J. Phys. Chem. A* 111 (2007) 12702–12710.
- [153] J.X. Wang, F.A. Uribe, T.E. Springer, J. Zhang, R.R. Adzic, *Faraday Discuss.* 140 (2009) 347–362.
- [154] R. Ferrando, J. Jellinek, R.L. Johnston, *Chem. Rev.* 108 (2008) 845–910.
- [155] W. Yu, M.D. Porosoff, J.G. Chen, *Chem. Rev.* 112 (2012) 5780–5817.
- [156] L. Yang, M.B. Vukmirovic, D. Su, K. Sasaki, J.A. Herron, M. Mavrikakis, S. Liao, R.R. Adzic, *J. Phys. Chem. C* 117 (2012) 1748–1753.
- [157] A.V. Ruban, H.L. Skriver, J.K. Nørskov, *Phys. Rev. B* 59 (1999) 15990–16000.
- [158] J.-H. Liu, A.-Q. Wang, Y.-S. Chi, H.-P. Lin, C.-Y. Mou, *J. Phys. Chem. B* 109 (2004) 40–43.
- [159] A.-Q. Wang, J.-H. Liu, S.D. Lin, T.-S. Lin, C.-Y. Mou, *J. Catal.* 233 (2005) 186–197.
- [160] A.-Q. Wang, C.-M. Chang, C.-Y. Mou, *J. Phys. Chem. B* 109 (2005) 18860–18867.
- [161] A. Wang, Y.-P. Hsieh, Y.-F. Chen, C.-Y. Mou, *J. Catal.* 237 (2006) 197–206.
- [162] C.-W. Yen, M.-L. Lin, A. Wang, S.-A. Chen, J.-M. Chen, C.-Y. Mou, *J. Phys. Chem. C* 113 (2009) 17831–17839.
- [163] T. Fujita, P. Guan, K. McKenna, et al., *Nat. Mater.* 11 (2012) 775–780.
- [164] J.J. Pireaux, M. Chtailb, J.P. Delrue, P.A. Thiry, M. Liehr, R. Caudano, *Surf. Sci.* 141 (1984) 211–220.
- [165] N. Saliba, D.H. Parker, B.E. Koel, *Surf. Sci.* 410 (1998) 270–282.
- [166] J. Kim, E. Samano, B.E. Koel, *Surf. Sci.* 600 (2006) 4622–4632.
- [167] J. Gong, D.W. Flaherty, R.A. Ojifinni, J.M. White, C.B. Mullins, *J. Phys. Chem. C* 112 (2008) 5501–5509.
- [168] L.V. Moskaleva, S. Rohe, A. Wittstock, V. Zielasek, T. Kluner, K.M. Neyman, M. Baumer, *PCCP* 13 (2011) 4529–4539.
- [169] L. Deng, W. Hu, H. Deng, S. Xiao, J. Tang, *J. Phys. Chem. C* 115 (2011) 11355–11363.

- [170] E. Ringe, R.P. Van Duyne, L.D. Marks, *Nano Lett.* 11 (2011) 3399–3403.
- [171] J. Lin, A. Wang, B. Qiao, X. Liu, X. Yang, X. Wang, J. Liang, J. Li, J. Liu, T. Zhang, *J. Am. Chem. Soc.* 135 (2013) 15314–15317.
- [172] A. Uzun, V. Ortolan, Y. Hao, N.D. Browning, B.C. Gates, *J. Phys. Chem. C* 113 (2009) 16847–16849.
- [173] H. Zhang, T. Watanabe, M. Okumura, M. Haruta, N. Toshima, *Nat. Mater.* 11 (2012) 49–52.
- [174] J.S. Jirkovský, I. Panas, E. Ahlberg, M. Halasa, S. Romani, D.J. Schiffrin, *J. Am. Chem. Soc.* 133 (2011) 19432–19441.
- [175] S. Sun, G. Zhang, N. Gauquelin, et al., *Sci. Rep.* 3 (2013).
- [176] J.M. Thomas, R. Raja, D.W. Lewis, *Angew. Chem. Int. Ed.* 44 (2005) 6456–6482.
- [177] M. Ranocchiari, C. Lothschütz, D. Grolimund, J.A. van Bokhoven, *Proc. Roy. Soc. A: Math. Phys. Eng. Sci.* 468 (2012) 1985–1999.
- [178] M. Flytzani-Stephanopoulos, B.C. Gates, *Annu. Rev. Chem. Biomol. Eng.* 3 (2012) 545–574.
- [179] S.F.J. Hackett, R.M. Brydson, M.H. Gass, I. Harvey, A.D. Newman, K. Wilson, A.F. Lee, *Angew. Chem. Int. Ed.* 46 (2007) 8593–8596.
- [180] Y.-T. Kim, K. Ohshima, K. Higashimine, T. Uruga, M. Takata, H. Suematsu, T. Mitani, *Angew. Chem. Int. Ed.* 45 (2006) 407–411.
- [181] Q. Fu, H. Saltsburg, M. Flytzani-Stephanopoulos, *Science* 301 (2003) 935–938.
- [182] K.T. Rim, D. Eom, L. Liu, E. Stolyarova, J.M. Raitano, S.-W. Chan, M. Flytzani-Stephanopoulos, G.W. Flynn, *J. Phys. Chem. C* 113 (2009) 10198–10205.
- [183] T.K. Ghosh, N.N. Nair, *ChemCatChem* 5 (2013) 1811–1821.
- [184] Z. Hu, H. Metiu, *J. Phys. Chem. C* 115 (2011) 17898–17909.
- [185] V. Shapovalov, H. Metiu, *J. Catal.* 245 (2007) 205–214.
- [186] W. Song, A.P.J. Jansen, E.J.M. Hensen, *Faraday Discuss.* 162 (2013) 281–292.
- [187] X. Liu, K. Zhou, L. Wang, B. Wang, Y. Li, *J. Am. Chem. Soc.* 131 (2009) 3140–3141.
- [188] C. Zhang, A. Michaelides, D.A. King, S.J. Jenkins, *J. Phys. Chem. C* 113 (2009) 6411–6417.
- [189] D. Pierre, W. Deng, M. Flytzani-Stephanopoulos, *Top. Catal.* 46 (2007) 363–373.
- [190] J.H. Kwak, J. Hu, D. Mei, C.-W. Yi, D.H. Kim, C.H.F. Peden, L.F. Allard, J. Szanyi, *Science* 325 (2009) 1670–1673.
- [191] M. Moses-DeBusk, M. Yoon, L.F. Allard, D.R. Mullins, Z. Wu, X. Yang, G. Veith, G.M. Stocks, C.K. Narula, *J. Am. Chem. Soc.* 135 (2013) 12634–12645.
- [192] Z. Huang, X. Gu, Q. Cao, P. Hu, J. Hao, J. Li, X. Tang, *Angew. Chem. Int. Ed.* 51 (2012) 4198–4203.
- [193] C. Zhang, F. Liu, Y. Zhai, H. Ariga, N. Yi, Y. Liu, K. Asakura, M. Flytzani-Stephanopoulos, H. He, *Angew. Chem. Int. Ed.* 51 (2012) 9628–9632.
- [194] S. Wang, A.Y. Borisevich, S.N. Rashkeev, M.V. Glazoff, K. Sohlberg, S.J. Pennycook, S.T. Pantelides, *Nat. Mater.* 3 (2004) 143–146.
- [195] T.-Y. Chang, Y. Tanaka, R. Ishikawa, K. Toyoura, K. Matsunaga, Y. Ikuhara, N. Shibata, *Nano Lett.* 14 (2013) 134–138.
- [196] A.L. Linsebigler, G. Lu, J.T. Yates, *Chem. Rev.* 95 (1995) 735–758.
- [197] A. Fujishima, X. Zhang, D. Tryk, *Surf. Sci. Rep.* 63 (2008) 515–582.
- [198] K. Nakata, A. Fujishima, *J. Photoch. Photobio. C* 13 (2012) 169–189.
- [199] U. Diebold, *Surf. Sci. Rep.* 48 (2003) 53–229.
- [200] S.-C. Li, L.-N. Chu, X.-Q. Gong, U. Diebold, *Science* 328 (2010) 882–884.
- [201] U. Diebold, S.-C. Li, M. Schmid, *Annu. Rev. Phys. Chem.* 61 (2010) 129–148.
- [202] H. Iddir, V. Skavysh, S. Ögüt, N.D. Browning, M.M. Disko, *Phys. Rev. B* 73 (2006) 041403.
- [203] V. Çelik, H. Ünal, E. Mete, Ş. Ellialtıoğlu, *Phys. Rev. B* 82 (2010) 205113.
- [204] X.G. Wang, W. Weiss, S.K. Shaikhutdinov, M. Ritter, M. Petersen, F. Wagner, R. Schlögl, M. Scheffler, *Phys. Rev. Lett.* 81 (1998) 1038–1041.
- [205] S. Yamamoto, T. Kendelewicz, J.T. Newberg, et al., *J. Phys. Chem. C* 114 (2010) 2256–2266.
- [206] J. Jin, X. Ma, C.Y. Kim, D.E. Ellis, M.J. Bedzyk, *Surf. Sci.* 601 (2007) 3082–3098.
- [207] L. Maïke, M. Wolfgang, *J. Phys. Condens. Matter* 21 (2009) 134010.
- [208] E. Wasserman, J.R. Rustad, A.R. Felmy, B.P. Hay, J.W. Halley, *Surf. Sci.* 385 (1997) 217–239.
- [209] S. Thevuthasan, Y.J. Kim, S.I. Yi, S.A. Chambers, J. Morais, R. Denecke, C.S. Fadley, P. Liu, T. Kendelewicz, G.E. Brown Jr., *Surf. Sci.* 425 (1999) 276–286.
- [210] V. Ortolan, A. Uzun, B.C. Gates, N.D. Browning, *Nat. Nanotechnol.* 5 (2010) 506–510.
- [211] J. Lu, C. Aydin, N.D. Browning, B.C. Gates, *Angew. Chem. Int. Ed.* 51 (2012) 5842–5846.

- [212] Y. Kondo, K. Yagi, K. Kobayashi, H. Kobayashi, Y. Yanaka, K. Kise, T. Ohkawa, *Ultramicroscopy* 36 (1991) 142–147.
- [213] K. Yagi, *Surf. Sci. Rep.* 17 (1993) 307–362.
- [214] A.K. Petford, L.D. Marks, M. O’Keeffe, *Surf. Sci.* 172 (1986) 496–508.
- [215] W.M.J. Coene, A. Thust, M. Op de Beeck, D. Van Dyck, *Ultramicroscopy* 64 (1996) 109–135.
- [216] C.L. Jia, A. Thust, *Phys. Rev. Lett.* 82 (1999) 5052–5055.
- [217] A. Thust, *Phys. Rev. Lett.* 102 (2009) 220801.
- [218] A. Thust, W.M.J. Coene, M. Op de Beeck, D. Van Dyck, *Ultramicroscopy* 64 (1996) 211–230.
- [219] Y. Shidahara, K. Aoki, Y. Tanishiro, H. Minoda, K. Yagi, *Surf. Sci.* 357–358 (1996) 820–824.
- [220] A.V. Crewe, J. Wall, J. Langmore, *Science* 168 (1970) 1338–1340.
- [221] E. Zeitler, M.G.R. Thomson, *Optik* 31 (1970) 258.
- [222] A.V. Crewe, *J. Microsc.-Oxf* 100 (1974) 247–259.
- [223] J. Wall, J. Langmore, M. Isaacson, A.V. Crewe, *Proc. Natl. Acad. Sci.* 71 (1974) 1–5.
- [224] V. Beck, A.V. Crewe, *Ultramicroscopy* 1 (1975) 137–144.
- [225] M. Isaacson, D. Kopf, M. Utlaut, N.W. Parker, A.V. Crewe, *Proc. Natl. Acad. Sci.* 74 (1977) 1802–1806.
- [226] J.S. Wall, *Chem. Scr.* 14 (1979) 271–278.
- [227] L.A. Freeman, A. Howie, M.M.J. Treacy, *J. Microsc.-Oxf* 111 (1977) 165–178.
- [228] M.M.J. Treacy, A. Howie, C.J. Wilson, *Philos. Mag. A* 38 (1978) 569–585.
- [229] K. Tsutomu, *Jpn. J. Appl. Phys.* 7 (1968) 27.
- [230] D. Cherns, *Philos. Mag.* 30 (1974) 549–556.
- [231] G. Lehmpfuhl, Y. Uchida, *Ultramicroscopy* 4 (1979) 275–282.
- [232] K. Yagi, K. Takayanagi, K. Kobayashi, N. Osakabe, Y. Tanishiro, G. Honjo, *Surf. Sci.* 86 (1979) 174–181.
- [233] S. Iijima, *Ultramicroscopy* 6 (1981) 41–52.
- [234] Y. Tanishiro, H. Kanamori, K. Takayanagi, K. Yagi, G. Honjo, *Surf. Sci.* 111 (1981) 395–413.
- [235] K. Takayanagi, *Ultramicroscopy* 8 (1982) 145–161.
- [236] K. Yagi, *Scanning Electron Microsc.* (1982) 1421–1428.
- [237] A.F. Moodie, C.E. Warble, *Philos. Mag.* 16 (1967) 891.
- [238] L.D. Marks, *Phys. Rev. Lett.* 51 (1983) 1000–1002.
- [239] L.D. Marks, *Acta Crystallogr. Sect. A* 40 (1984) C390.
- [240] L.D. Marks, *Surf. Sci.* 139 (1984) 281–298.
- [241] K. Abdelmoula, J.J. Metois, G. Nihoul, *Phys. Status Solidi A–Appl. Res.* 77 (1983) K5.
- [242] K. Takayanagi, K. Yagi, *Trans. Jpn. Inst. Metals* 24 (1983) 337–348.
- [243] G. Nihoul, K. Abdelmoula, J.J. Metois, *Ultramicroscopy* 12 (1984) 353–366.
- [244] J.M. Gibson, M.L. McDonald, F.C. Unterwald, *Phys. Rev. Lett.* 55 (1985) 1765–1767.
- [245] S.A. Nepijko, T.N. Bondarenko, H. Hofmeister, *J. Cryst. Growth* 71 (1985) 735–738.
- [246] P. Lu, D.J. Smith, *Phys. Rev. Lett.* 59 (1987) 2177–2179.
- [247] M. Shiojiri, T. Isshiki, K. Okashita, Y. Hirota, T. Maeda, S. Sekimoto, *Ultramicroscopy* 23 (1987) 355–363.
- [248] M. Shiojiri, T. Isshiki, Y. Hirota, *Ultramicroscopy* 30 (1989) 329–336.
- [249] D.J. Smith, R. W. Glaisher, P. Lu, M.R. McCartney, *Ultramicroscopy* 29 (1989) 123–134.
- [250] K. Takayanagi, *J. Electron Microsc.* 38 (1989) S58–S65.
- [251] M. Mitome, K. Takayanagi, Y. Tanishiro, *Ultramicroscopy* 33 (1990) 255–260.
- [252] X.G. Ning, H.Q. Ye, *Philos. Mag. A* 62 (1990) 431–446.
- [253] P. Lu, D.J. Smith, *Surf. Sci.* 254 (1991) 119–124.
- [254] T. Isshiki, M. Toyoshima, M. Tsujikura, H. Saijo, M. Shiojiri, *Ultramicroscopy* 41 (1992) 201–209.
- [255] K. Yagi, *J. Electron Microsc.* 44 (1995) 269–280.
- [256] T. Mishima, T. Osaka, *Surf. Sci.* 395 (1998) L256–L260.
- [257] L.D. Marks, *Rep. Prog. Phys.* 57 (1994) 603.
- [258] L.D. Marks, *Surf. Sci.* 139 (1984) 281–298.
- [259] M. Mitome, K. Takayanagi, Y. Tanishiro, *Phys. Rev. B* 42 (1990) 7238–7241.
- [260] C.-C. Chen, C. Zhu, E.R. White, C.-Y. Chiu, M.C. Scott, B.C. Regan, L.D. Marks, Y. Huang, J. Miao, *Nature* 496 (2013) 74–77.